





Pattern selection for thermocapillary flow in rectangular containers in microgravity

P. Salgado Sánchez ^{*}, J. Porter , J. M. Ezquerro , I. Tínao, and A. Laverón-Simavilla 
E-USOC, Center for Computational Simulation, Escuela Técnica Superior de Ingeniería Aeronáutica y del Espacio, Universidad Politécnica de Madrid, Plaza Cardenal Cisneros 3, 28040 Madrid, Spain



(Received 26 November 2021; accepted 21 April 2022; published 9 May 2022)

A detailed numerical investigation of pattern selection for thermocapillary flow in rectangular containers in microgravity is presented. These dynamics are studied for liquid *n*-octadecane, an alkane with high Prandtl number ($Pr = 52.53$), due to its relevance to recent microgravity experiments. Pattern selection is analyzed in terms of the aspect ratio, Γ , and the applied Marangoni number, Ma . In short containers, the bifurcation picture is characterized by a transition from steady thermocapillary flow to a standing wave (SW) oscillatory mode as Ma is varied. This transition takes the form of a primary subcritical Hopf bifurcation accompanied by a secondary saddle node; these two bifurcations delimit a region of bistability. In large containers, the dynamics is characterized by a supercritical Hopf bifurcation that marks the transition from steady flow to a traveling wave (TW) mode. The critical Ma for this transition increases with Γ . In intermediate containers, a complex pattern selection scenario is found, where both steady and oscillatory convection, in the form of either TWs or SWs, can appear depending on Γ and Ma . Finally, we apply this bifurcation analysis to help explain recent results on thermocapillary flows during the melting of phase change materials in microgravity [Salgado Sánchez *et al.*, *Int. J. Heat Mass Transf.* **163**, 120478 (2020); Salgado Sánchez *et al.*, *J. Fluid Mech.* **908**, A20 (2021)]. The temporal evolution of the phase change is characterized by an effective Γ and Ma in the liquid phase. We find very good agreement between the flow transitions observed during melting and those predicted for the equivalent rectangular containers over the explored range of $1.5 \leq \Gamma \leq 16$.

DOI: [10.1103/PhysRevFluids.7.053502](https://doi.org/10.1103/PhysRevFluids.7.053502)

I. INTRODUCTION

Thermocapillary flows have attracted sustained interest from the scientific community due to their relevance in many important technological processes such as crystal growth [1–3], combustion [4,5] and welding [6–8], and in other phenomena like the migration of bubbles and the spreading of drops [9–12]. During the growth (solidification) of crystals, in particular, there is now a general consensus that flows driven by the thermocapillary effect can interact with the solidification front, resulting in complex dynamics that critically affect crystal quality. Such analyses have focused on two fundamental geometries, cylindrical liquid bridges, and rectangular containers, as models of the floating-zone and the open-boat techniques, respectively.

In rectangular containers, the streamwise aspect ratio Γ is the key parameter that selects the character of the flow [13]. In short containers with $\Gamma \sim O(1)$, the flow is typically dominated by a single vortex. One of the first numerical investigations of this limit was carried out by Zebib *et al.* [14], who analyzed the thermocapillary flow in a square cavity in the absence of natural convection. They not only clarified the single-vortex flow structure, but also examined the scaling

*pablo.salgado@upm.es

of the boundary layers and the free-surface deformations at leading order; these results were later extended by Carpenter and Homsy [15]. The numerical work of Peltier and Biringen [16] was the first to show oscillatory behavior in a two-dimensional rectangular domain with $\Gamma \simeq 2.3$ for a moderate Prandtl number (Pr) of 6.8. Their results indicate that the heated lateral boundaries have a strong stabilizing effect on the onset of two-dimensional oscillations.

In the case of large containers ($\Gamma \gg 1$), the basic steady solution is the *return flow* state, obtained by Sen and Davis [17] using asymptotic techniques; the validity of this solution was later checked against numerical simulations in large but finite containers [18]. Motivated by the seminal experiments of Schwabe and Scharmann [2] and Chub and Wuest [19], who observed oscillatory thermocapillary flows for the first time, Smith and Davis [20] analyzed the stability of the return flow solution using linear theory and demonstrated the existence of oscillatory oblique (i.e., three-dimensional) *hydrothermal waves* propagating from the cold side of the cavity. For liquids of high Pr, these hydrothermal waves were shown to be (nearly) two-dimensional and supported by vertical gradients in the liquid domain [21]. The return flow, however, can become unstable prior to the onset of hydrothermal waves. Depending on parameters, a sequence of steady corotating vortices may penetrate into the interior from the walls [22,23]. A more general stability analysis of the return flow state was conducted by Priede and Gerbeth [24], who considered both absolute and convective instabilities and showed that the return flow can become unstable (globally) to two-dimensional corotating vortices.

There has been continued interest (see, e.g., [13,25] and references therein) in thermocapillary flows since these early pioneering investigations. However, only a handful of theoretical studies (that the authors are aware of) have considered the coupling between thermocapillary flows and the dynamic boundary conditions generated by the *moving* solid/liquid front during melting or solidification in microgravity. The first systematic attempt was the recent work of Salgado Sánchez *et al.* [26], which analyzed the thermocapillary flows that appear in the liquid phase during melting from the complementary perspectives of pattern formation and fluid mechanics. Various regimes depending on the applied Marangoni number (Ma) and Γ were identified in terms of the bifurcations separating them. Both steady and oscillatory modes—either having the appearance of traveling or (approximately) standing waves—were found. The critical boundaries between them were determined and discussed in terms of the effective aspect ratio of the liquid domain. In the large Γ limit, the work of Lappa [3] on the formation of hydrothermal waves in a large container during the solidification of succinonitrile is also relevant.

Although not directly focused on aspects of pattern formation, the recent numerical work of Madruga and Mendoza [27,28] on thermocapillary flows was the first to suggest the positive effect of thermocapillary convection on heat transport during the melting of phase change materials (PCMs) in microgravity. These predictions were then confirmed by the parabolic flight experiments of Ezquerro *et al.* [29,30], which observed for the first time the melting of a PCM (*n*-octadecane) in rectangular containers with a free surface. Salgado Sánchez *et al.* [31] complemented these results by experimentally and numerically examining the effect of the container aspect ratio for $\Gamma \in [1, 1.66]$, i.e., near the $\Gamma \sim O(1)$ limit. The work of Salgado Sánchez *et al.* [32] extended these results to $\Gamma \gg 1$ and also investigated the transitional behavior at intermediate aspect ratios. It was seen that, for large containers, the thermocapillary effect can enhance heat transport by up to a factor of 20, depending on Ma. For short containers, the enhancement factor was on the order of 5 when oscillatory flow was present. As noted above, only a few theoretical studies (see, e.g., [33–36] and references therein) considered the influence of thermocapillary flow on phase changes.

Recent interest in the effect of thermocapillary flow on PCM performance in microgravity is motivated by the special and demanding conditions of space missions, where significant unwanted temperature variations can result from varying radiation exposure and the waste heat generated by onboard systems. PCMs are attractive for their low maintenance and simplicity, and their ability to store and release large amounts of energy near the phase transition temperature T_M . In ordinary use (on Earth) they help control temperatures and improve performance in a wide range of systems including air conditioning, electronics, manufacturing, food storage, construction, and solar energy.

Among the range of possible materials for PCM devices in space applications, organic PCMs like alkanes are particularly appealing due to their stability and convenient operating temperatures. Their effectiveness can be limited, however, by low thermal conductivity and the resulting lag in response time.

Several strategies have been pursued to reduce the response time of PCM devices. For example, one can modify the effective thermal conductivity through the addition of more conductive material [37–41]. However, with the exception of nano-enhanced PCMs using dispersed nanoparticles [42,43], this approach requires increased mass and/or volume, which is of particular concern in space missions. Alternatively, convective flows in the liquid phase can significantly enhance the performance of PCMs, even without modifying conductivity. While buoyancy-driven convection can be exploited on ground [44–49], the thermocapillary effect stands out as the only simple alternative in microgravity [50–54]. If the PCM design incorporates a free surface, the temperature gradient inherent to its operation induces variations in surface tension that drive convective flow. Furthermore, the presence of the gas layer helps alleviate the problem of disruptive pressure changes (and related bubbles/voids) associated with the thermal expansion of the material during its melting/solidification.

As a specific motivation, we note that the potential for thermocapillary flows to improve the performance of PCM devices in space applications will be experimentally evaluated by the Marangoni Phase Change Materials (MarPCM) project [55] during a planned series of microgravity experiments on board the International Space Station. These experiments will investigate cuboidal and cylindrical configurations with a free (thermocapillary) surface during complete melting and solidification cycles of the alkane *n*-octadecane, as well as a nano-enhanced material. The detailed analysis provided here of pattern selection in rectangular containers of liquid *n*-octadecane in microgravity is an important part of the effort to predict and explain the dynamics that are expected to be observed experimentally.

The manuscript is structured as follows. In Sec. II the model describing thermocapillary flow in a rectangular container is described, with emphasis on the governing dimensionless parameters, the numerical implementation and the approach used to conduct the bifurcation analysis of the system. In Sec. III the pattern selection results are summarized with a stability map in terms of Γ and Ma . This is complemented by bifurcation diagrams, spectrograms, and a detailed analysis of the flow for selected values of Γ that are representative of short, large, and intermediate containers in Secs. III A, III B, and III C, respectively. The results are then used in Sec. IV to explain the dynamics observed during the melting of *n*-octadecane in microgravity. Here the formulation used to resolve the phase change is revised, and specific cases are analyzed in terms of an effective Ma and Γ . Final conclusions are given in Sec. V.

II. MATHEMATICAL FORMULATION

We consider an open two-dimensional rectangular container of liquid that is subjected to a temperature difference ΔT applied at opposite lateral walls. Along the upper boundary, which is assumed flat and adiabatic, the applied temperatures induce gradients in surface tension that drive thermocapillary flow.

A. Governing equations and boundary conditions

The Navier-Stokes equations for laminar and incompressible flow [56] are used to describe the conservation of mass, momentum and energy in the fluid:

$$\nabla \cdot \mathbf{u} = 0, \quad (1a)$$

$$\rho \left[\frac{\partial \mathbf{u}}{\partial t} + (\mathbf{u} \cdot \nabla) \mathbf{u} \right] = -\nabla p + \nabla(\mu \nabla \mathbf{u}), \quad (1b)$$

$$\rho c_p \left(\frac{\partial T}{\partial t} + \mathbf{u} \cdot \nabla T \right) = \nabla(k \nabla T), \quad (1c)$$

where \mathbf{u} , p , and T are the velocity, pressure and temperature fields, and ρ , μ , c_p , and k refer to the liquid density, dynamic viscosity, heat capacity at constant pressure, and thermal conductivity.

The thermocapillary effect is considered in the linear approximation, where the interfacial tension σ depends on temperature as

$$\sigma = \sigma_0 - \gamma (T - T_0). \quad (2)$$

Here the thermocapillary coefficient $\gamma = |\partial\sigma/\partial T|$ characterizes the variation of σ with respect to the reference value σ_0 at temperature T_0 . This variation in σ provides the driving force for convection by pulling the liquid along the surface from regions of lower to higher surface tension.

As the temperature gradient at the open boundary generates thermocapillary convection, there is a balance between pressure, viscous stresses, and surface tension. For simplicity, we assume a contact angle of $\beta = \pi/2$ and a perfectly flat interface. Thus, the only dependence on σ is through the thermocapillary coefficient and the balance simplifies to

$$\mu \nabla_n \mathbf{u}_t = -\gamma \nabla_t T, \quad (3)$$

where the subscripts n and t refer to normal and tangential components, respectively.

The remaining boundary conditions for T and \mathbf{u} are as follows:

(1) Along the left ($x = 0$) and right ($x = L$) lateral walls, isothermal and no-slip conditions hold:

$$T = T_0 + \Delta T \text{ (at } x = 0\text{)}, \quad T = T_0 \text{ (at } x = L\text{)}; \quad \mathbf{u} = 0. \quad (4)$$

(2) Along the bottom wall ($y = 0$), adiabatic and no-slip conditions are applied:

$$\nabla_n T = 0; \quad \mathbf{u} = 0. \quad (5)$$

(3) Along the surface ($y = H$), the balance of Eq. (3) between viscous and thermocapillary stress is combined with adiabatic temperature and slip velocity conditions:

$$\nabla_n T = 0; \quad \mathbf{u}_n = 0. \quad (6)$$

These boundary conditions are indicated in Fig. 1; the use of perfectly adiabatic boundaries is consistent with previous analyses (see, e.g., Sen and Davis [17]).

B. Dimensionless parameters

We rescale length with L , time with L^2/α , where $\alpha = k/(\rho c_p)$ is the liquid thermal diffusivity, and temperature with ΔT :

$$(\hat{\mathbf{x}}, \tau, \Theta) = \left(\frac{\mathbf{x}}{L}, t \frac{\alpha}{L^2}, \frac{T - T_0}{\Delta T} \right).$$

The dynamics of Eqs. (1)–(6) depend on the Marangoni number

$$\text{Ma} = \frac{\gamma L \Delta T}{\mu \alpha}, \quad (7)$$

which quantifies the relative importance for heat transport of the thermocapillary effect compared to thermal diffusion, the Prandtl number

$$\text{Pr} = \frac{\mu}{\rho \alpha}, \quad (8)$$

which is the ratio between the diffusion of momentum and heat, and the container aspect ratio

$$\Gamma = \frac{L}{H}, \quad (9)$$

which characterizes the geometry.

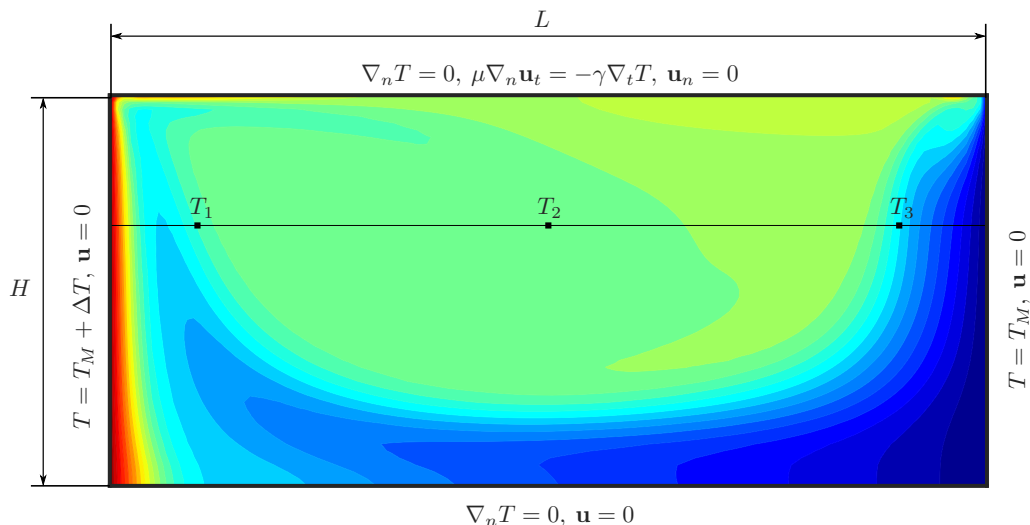


FIG. 1. Sketch of the two-dimensional numerical model considered: an open rectangular container of length L and height H holding liquid n -octadecane ($Pr = 52.53$) subjected to isothermal conditions along its lateral walls and adiabatic ones at the top and bottom boundaries. The temperatures T_1 , T_2 , and T_3 are measured at the indicated points, which are a distance $2H/3$ up from the bottom and separated from the left wall by $L/10$, $L/2$, and $9L/10$, respectively.

We resolve the dynamics of liquid n -octadecane because of its relevance to upcoming microgravity experiments [55] and to recent work on the effect of thermocapillary flows during melting [26,29–32]. The relevant physical properties of this alkane are summarized in Table I, while the melting temperature T_M is taken as the reference value T_0 .

Previous analytical studies of thermocapillary flows in rectangular containers [17,18] found that interface deformation had a negligible effect on the qualitative aspects of the flow structure, which is the focus of the present work. Furthermore, experimental [57] and numerical [58] analyses of liquid bridges have reported that the free surface deformation caused by thermocapillary flow is proportional to the capillary number

$$Ca = \frac{\gamma \Delta T}{\sigma_0}. \quad (10)$$

For n -octadecane, with a surface tension value of approximately $\sigma_0 \simeq 27$ mN/m [59] at its melting temperature, $Ca \leq 0.12$ and the free surface deformation is expected to be on the order of microns [57].

TABLE I. Physical properties of liquid n -octadecane, reproduced from Ref. [31].

Melting temperature, T_M	28 °C
Density, ρ	780 kg/m ³
Heat capacity at constant pressure, c_p	2196 J/(kg K)
Thermal conductivity, k	0.15 W/(m K)
Dynamic viscosity, μ	3.54×10^{-3} Pa s
Thermocapillary coefficient, γ	8.44×10^{-5} N/(m K)

TABLE II. Nondimensional parameters explored, corresponding to a temperature difference $\Delta T \in (0, 40]$ K, container height $H \in [1.125, 15]$ mm, and the properties of *n*-octadecane.

Ma	Γ	Ca	Pr
(0, 248 298]	(1, 22.8]	(0, 0.12]	52.53

The assumption of two-dimensional dynamics is justified to some extent by the high Prandtl number ($\text{Pr} = 52.53$) of *n*-octadecane, which was shown to lead to essentially two-dimensional thermocapillary flows [13,16,20]. We focus here on this choice of PCM and a range of temperatures satisfying $\Delta T \leq 40$ K, which is the maximum applied temperature difference planned for the MarPCM experiments [55]. Fluids with larger Pr, such as high viscosity silicone oils, would require temperature differences well above that range to observe transitions in the flow dynamics. Fluids with lower Pr, on the other hand, are associated with larger thermal diffusivity and, thus, diminished importance for thermocapillary effects.

C. Numerical implementation

COMSOL Multiphysics is used to solve the governing equations (1) with the set of boundary conditions (3)–(6) in dimensional variables using the finite element method.

The initial condition for the temperature field is $T = T_M$ so that there is no driving force for fluid motion and, thus, the liquid is assumed motionless with $\mathbf{u} = 0$. The temperature difference ΔT is introduced to the system using linear profiles (ramps) characterized by the heating rate ε (slope) as

$$\Delta T = \varepsilon t. \quad (11)$$

After reaching the maximum $\Delta T = 40$ K considered in this work, the system is maintained for several seconds at that thermal setting until it reaches a stationary (constant-amplitude) solution if the flow is steady (oscillatory). Then ΔT is decreased again to zero; Eq. (11) describes this linear cooling at a rate $\varepsilon < 0$ after an appropriate shift in ΔT and time.

To explore different values of Γ , we follow Ref. [16] and vary the container height H for a fixed length of $L = 22.5$ mm as in the experiments of Ref. [55]; this is also consistent with the procedure followed in Refs. [26,32]. Each simulation is thus performed at constant Γ with a variable temperature profile, as described above. The range of nondimensional parameters explored is summarized in Table II.

The temporal evolution is effected with a Backward Differentiation Formulae scheme together with streamline [60] and crosswind [61] stabilization techniques to avoid spurious numerical oscillations. We use a maximum mesh size of $(2/3)\mathcal{S}$ if $\Gamma \geq 4.5$, and \mathcal{S} if $\Gamma < 4.5$ where $\mathcal{S} = L/67.5$, consistent with the selection of Refs. [26,31,32], where a convergence analysis is provided and simulations are validated against experiments. The time step is set to $\Delta t = 10^{-2}$ s, but can be reduced automatically according to the Courant-Friedrichs-Levy convergence condition for numerical stability.

In this work, the thermocapillary flows in an ideal rectangular container (see Fig. 1) are compared to the flows observed during melting in rectangular containers in microgravity; see Sec. IV. The fact that the progression of the solid/liquid front during melting modifies the effective Γ and Ma in the liquid phase was discussed in Ref. [26], where the phase change was studied under isothermal conditions with $T_M + \Delta T$ and T_M imposed at the respective lateral walls. During the initial stage of the melting process, the characteristic (effective) length of the liquid phase, L_{eff} , is small and, consequently, so is the associated aspect ratio, Γ_{eff} , and the effective Marangoni number, Ma_{eff} . As the melting progresses, L_{eff} increases until it takes the value of the container length L and Ma_{eff} reaches the nominal Ma. Similarly, Γ_{eff} evolves toward Γ . To model this type of variation in a fixed rectangular geometry, we increase the applied Ma by using piecewise linear profiles for ΔT . The

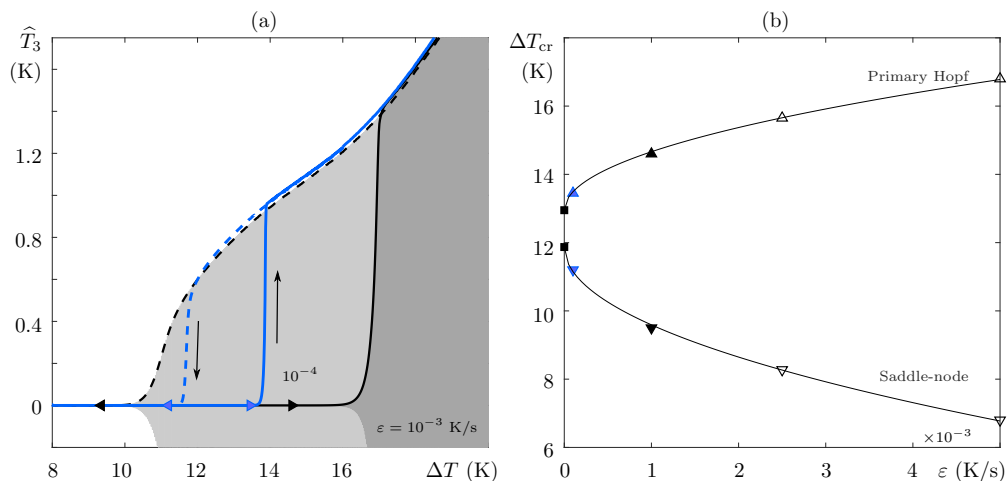


FIG. 2. (a) Bifurcation diagram showing the temperature deviation $\widehat{T}_3 = T_3 - \langle T_3 \rangle$, using two different rates ε . The dark (light) gray curve shows \widehat{T}_3 for a heating (cooling) rate of $\varepsilon = 10^{-3}$ K/s with the envelope of the oscillations highlighted with a solid (dashed) black curve. The blue envelopes correspond to $\varepsilon = 10^{-4}$ K/s. (b) Estimated critical temperatures of the primary subcritical Hopf (upright triangles) and saddle-node (downward triangles) bifurcations for different values of ε . These estimates are fit with functions of the form $\Delta T_{cr}(\varepsilon) = \Delta T_{cr}(0) + a\sqrt{\varepsilon}$ (solid curves) to permit the critical ($\varepsilon = 0$) values to be extracted (indicated with squares). This square-root dependence on ramp rate is typical of delayed transitions controlled by transients or small-amplitude noise [62–64].

effect of geometry is considered separately using a wide range of Γ that covers the values explored in Ref. [26] during the phase change.

We note that this approach is just one among a variety of possibilities. For example, one could simultaneously vary the temperature at both lateral walls to achieve the same applied ΔT and start from an initial condition $T = T_M + \Delta T/2$. Another alternative would be to directly impose the desired ΔT between both lateral walls and use an ideal conductive profile $T = T_M + \Delta T(1 - x/L)$ for the initial temperature field. Since the selected pattern may depend critically on this initial condition, it is important for comparison presented in Sec. IV that it approximates the conditions present during the melting process.

D. Methods for stability analysis

In Sec. III, we present a full picture of pattern selection that includes the critical boundaries between different flow regimes over a wide range of Γ and Ma . Here we discuss the methods used to determine and characterize these bifurcations.

As noted above, the liquid is analyzed from an initially quiescent and isothermal state. The temperature difference ΔT is then increased at a rate of ε and, to diagnose qualitative changes in the flow, the temperatures T_1 , T_2 , and T_3 at three specific locations are monitored. These locations are $2/3$ of the way up from the bottom of the container at $x = L/10$, $x = L/2$ and $x = 9L/10$, respectively; see Fig. 1. After the temperature reaches the maximum value of 40 K, the simulation is run for a short time at constant ΔT and then, ΔT is decreased continuously to zero at a rate of $-\varepsilon$. This process is repeated for each value of Γ .

An example of the results obtained in this manner is provided in Fig. 2(a), which shows a bifurcation diagram in terms of the temperature deviation $\widehat{T}_3 = T_3 - \langle T_3 \rangle$, where angled brackets denote the temporal average over one oscillation period. Here the temperature is changed with a heating/cooling rate of $\varepsilon = \pm 10^{-3}$ K/s in a container of height $H = 13.5$ mm ($\Gamma \simeq 1.67$); the

dark (light) gray curve shows \widehat{T}_3 for increasing (decreasing) ΔT while the solid (dashed) black curves highlight the envelope of the oscillations. Note that the complete simulation, ramping up to $\Delta T = 40$ K then back down, requires a total time of approximately $2(\Delta T/\varepsilon) \approx 8 \times 10^4$ s (not including the short intermediate period at constant ΔT).

These bifurcation curves show that oscillatory flow appears and ceases at two critical values of ΔT that are consistent with hysteresis and a subcritical primary Hopf bifurcation. Repeating the same analysis with a smaller ramp rate of $\varepsilon = \pm 10^{-4}$ K/s (blue envelopes) shows a clear shift in both values of ΔT . While such a rate-dependent delay is generally not expected for simple steady or Hopf bifurcations in ordinary differential equations with a slowly varying parameter [65,66], it is consistent with transitions controlled by transients or small-amplitude noise [62–64] where the delay is proportional to the square root of the ramp rate—this follows from an ensemble-averaged estimate of the escape time for trajectories near the unstable solution. To analyze the error related to the ramping rate in this system, simulations were conducted using different values of ε and the critical values $\Delta T_{\text{cr}}(\varepsilon)$ were determined. The results, shown by markers in Fig. 2(b), can be fit to the predicted square root dependence using functions of the form $\Delta T_{\text{cr}}(\varepsilon) = \Delta T_{\text{cr}}(0) + a\sqrt{\varepsilon}$, where a is a constant and $\Delta T_{\text{cr}}(0)$ is the critical value at $\varepsilon = 0$; the limiting values are denoted below by $\Delta T_{\text{cr}}^{\text{H}}$ for the Hopf bifurcation and $\Delta T_{\text{cr}}^{\text{SN}}$ for the saddle-node bifurcation. The fact that $\Delta T_{\text{cr}}^{\text{H}}$ and $\Delta T_{\text{cr}}^{\text{SN}}$ differ is an indication that the hysteresis is not merely due to the delay effect, but also reflects the subcritical nature of the Hopf instability, something that will be discussed in more detail below along with the associated bistable regions.

The Hopf and saddle-node bifurcations are located, respectively, at $\Delta T_{\text{cr}}^{\text{H}} = 12.95$ K and $\Delta T_{\text{cr}}^{\text{SN}} = 11.87$ K. If a rate of $\varepsilon = 10^{-4}$ K/s is used, the observed critical values are $\Delta T_{\text{cr}}^{\text{H}}(\varepsilon) = 13.45$ K and $\Delta T_{\text{cr}}^{\text{SN}}(\varepsilon) = 11.22$ K, corresponding to errors of approximately 0.5 K. We remark that the values of $\Delta T_{\text{cr}}^{\text{H}}(\varepsilon)$ are determined from the modulation envelopes of the temperature signals, as they surpass an amplitude of 10^{-5} K, which is the absolute tolerance selected for the numerical solver.

A complete set of simulations were first performed with rates of $\varepsilon = 10^{-2}$ and 10^{-3} K/s to find the approximate locations of the critical curves; these will be shown later in Fig. 16 of Sec. IV. The calculations were then refined using a reduced rate of 10^{-4} K/s. Since the error associated with this ramp rate is on the order of 0.5 K, it may be presumed that the primary Hopf bifurcation is subcritical and accompanied by a saddle-node bifurcation when the estimated critical points with increasing and decreasing temperature differ by more than 0.5 K. If the difference is less than that, it may be explained by the delay (memory) effect and is consistent with a supercritical Hopf bifurcation. We further examine this bifurcation below to confirm its subcritical nature in particular cases.

III. PATTERN SELECTION: STABILITY MAP AND BIFURCATIONS

In this section, we analyze the thermocapillary-driven flow in rectangular containers in microgravity in terms of pattern selection and bifurcations. The stability map is first determined as a function of the governing parameters. Details of the flow and bifurcations in representative cases of short, large, and intermediate Γ containers are presented separately in the corresponding subsections. To facilitate physical interpretation and emphasize the connection with experiments, we present the results in dimensional variables while providing the associated dimensionless values in parentheses.

The stability map of Fig. 3 summarizes the three thermocapillary flow regimes in terms of the dimensional parameters H and ΔT (equivalently, the dimensionless parameters Γ and Ma). The critical boundaries separate steady flows and two modes of oscillatory convection: the standing wave mode (SW, blue curves) and the traveling wave mode (TW, red curves). Both SWs and TWs appear via a primary Hopf bifurcation that can be either supercritical or subcritical. In the latter case, this Hopf bifurcation is accompanied by a secondary saddle-node bifurcation. The Hopf and saddle-node bifurcations are labeled and indicated by solid and dashed curves, respectively, with circular markers denoting the values of H (Γ) explored in simulations. We describe these results

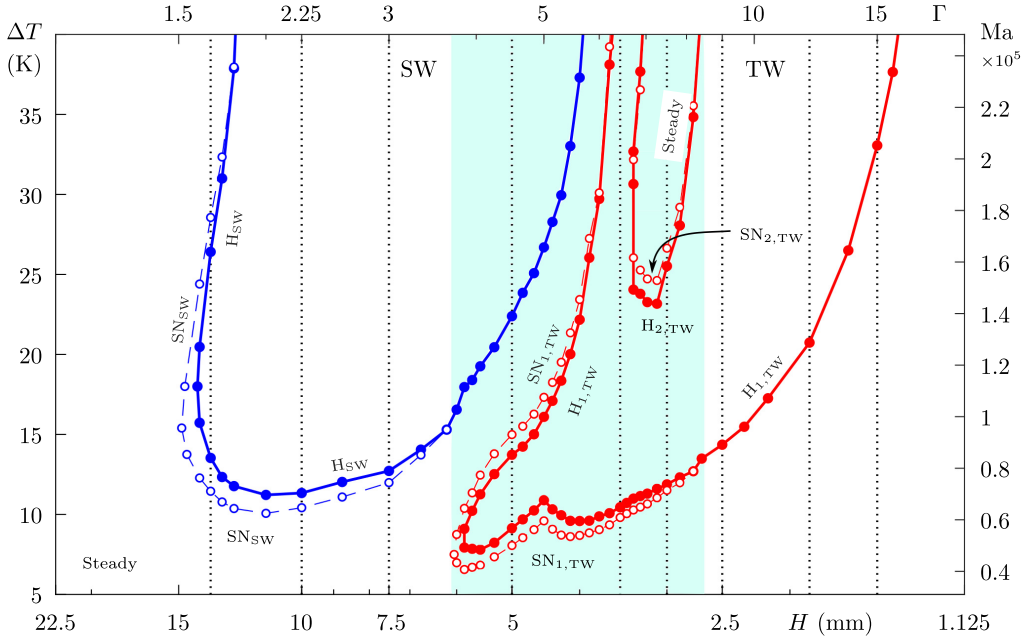


FIG. 3. Stability map in terms of H and ΔT (Γ and Ma are indicated on opposing axes) showing the critical boundaries for oscillatory thermocapillary flow in two regimes: standing wave (SW, blue) and traveling wave (TW, red). The Hopf (H) and saddle-node (SN) bifurcations are located by solid and dashed curves, respectively, with circular markers denoting the simulations. Dotted vertical lines mark the values of H (Γ) selected to illustrate the flow dynamics in small, large, and intermediate (shaded region) containers.

below in terms of Γ and Ma for ease of comparison with previous work where those parameters are standard [13].

In small (short/deep) containers with $H > 6.5$ mm [$\Gamma < 3.75 \sim O(1)$], the thermocapillary flow is steady at low values of ΔT . For $H \gtrsim 15$ mm ($\Gamma \lesssim 1.5$), i.e., beyond the leftmost point of the SN_{SW} curve, steady solutions remain stable and no oscillatory flow is found within the interval of ΔT explored. For $H < 15$ mm ($\Gamma > 1.5$), the initially steady flow at low ΔT undergoes a Hopf bifurcation (labeled as H_{SW}) to the SW mode as ΔT is increased. This primary bifurcation is found to be subcritical in this region and, thus, is accompanied by a secondary saddle-node bifurcation (SN_{SW}) and a small region of bistability (between the two curves) where both steady and periodic solutions exist at the same value of ΔT . The preceding flow (i.e., the initial condition) determines which solution is selected. In the vicinity of $H \simeq 6$ mm ($\Gamma \simeq 3.75$), the region of bistability narrows as the SN_{SW} curve collides with H_{SW} .

Depending on H , Hopf bifurcation can occur more than once. For example, with $H \simeq 13.5$ ($\Gamma \simeq 1.67$), marked by the leftmost vertical dotted line, the initially steady flow gives way to the SW mode near $\Delta T \simeq 13.53$ K ($Ma \simeq 8.40 \times 10^4$) but returns again at approximately $\Delta T \simeq 28.56$ K ($Ma \simeq 1.77 \times 10^5$) when the upper branch of the SN_{SW} curve is surpassed. When decreasing ΔT , the stable steady solutions at large ΔT lose their stability to SW along the upper branch of the primary Hopf bifurcation, but these SWs later disappear as ΔT falls below the lower SN_{SW} curve. The overall shape of the critical H_{SW} curve is consistent with the work of Peltier and Biringen [16], who analyzed thermocapillary flow in rectangular containers with $\Gamma \in [2.3, 3.8]$ holding a liquid of $Pr = 6.78$. A region was found with a double-valued critical boundary for $2.3 \leq \Gamma \leq 2.7$. Here we find a similar type of behavior for $1.5 < \Gamma < 1.8$ [$H \in (12.5, 15)$ mm]; the difference can be attributed to Pr , which is an order of magnitude larger. In this case, we also demonstrate the

subcritical nature of the primary Hopf instability, which is accompanied by a SN_{SW} bifurcation that stabilizes the initial branch of SW solutions at finite amplitude.

For intermediate containers with $H \in (2.75, 6.3)$ mm ($3.75 < \Gamma < 8$; blue shaded area in the figure), a more complex bifurcation picture is found. In containers with $H \in (3.75, 5.6)$ mm ($4 \lesssim \Gamma \lesssim 6$), the steady flow found at low ΔT becomes unstable to the TW mode as the primary Hopf curve $H_{1,\text{TW}}$ is crossed, which is subcritical in this region. The branch of unstable solutions created at this Hopf bifurcation is stabilized at finite amplitude through the saddle-node bifurcation $\text{SN}_{1,\text{TW}}$. With increasing ΔT , these stable TWs disappear in a second saddle-node bifurcation, located by the upper branch of $\text{SN}_{1,\text{TW}}$, where they collide with unstable periodic solutions created along the upper branch of $H_{1,\text{TW}}$. Again, the region between $H_{1,\text{TW}}$ and $\text{SN}_{1,\text{TW}}$ is bistable and either steady flow or TWs can be found at the same applied ΔT . As ΔT is raised beyond the upper $\text{SN}_{1,\text{TW}}$ curve, steady flow returns, persisting until the H_{SW} curve is crossed and the SW mode appears. The SW solutions in this large Ma region are stable, with no further bifurcations found over the explored interval.

In the vicinity of $H \simeq 3.75$ mm ($\Gamma \simeq 6$), the region of stable steady flow found at moderate Ma (i.e., between the $H_{1,\text{TW}}$ and H_{SW} curves) extends up to the maximum value of ΔT considered. Upon decreasing H (increasing Γ) a bit more, the system remains inside the upper part of the $H_{1,\text{TW}}$ curve and TWs are stable over a wide interval of ΔT : from their initial appearance near $\Delta T \simeq 9.61$ K ($\text{Ma} \simeq 5.97 \times 10^4$), up to the maximum explored value of 40 K. With further decrease (increase) in H (Γ), this extended region of stable TWs is interrupted by an isolated zone of steady solutions (labeled in Fig. 3) bounded by another subcritical Hopf bifurcation ($H_{2,\text{TW}}$) and an associated saddle node ($\text{SN}_{2,\text{TW}}$). The rightmost limit of this region near $H \simeq 2.8$ mm ($\Gamma \simeq 8$) marks the qualitative transition to the behavior typical of large containers. At approximately this same H value, the $\text{SN}_{1,\text{TW}}$ curve collides with the $H_{1,\text{TW}}$ curve (at $\Delta T \simeq 12.70$ K, $\text{Ma} \simeq 7.88 \times 10^4$), rendering the primary bifurcation supercritical for large containers.

Finally, in the region of $H < 2.8$ mm ($\Gamma > 8$), also referred to as large/shallow containers, the steady flow found at small to moderate ΔT loses stability to the TW mode as the temperature is raised past the $H_{1,\text{TW}}$ curve, which is now supercritical. With decreasing H , the critical ΔT for this transition to TWs is delayed.

To complete the stability analysis, additional details of the flow (natural frequency, amplitude, base flow, etc.) are presented in Secs. III A, III B, and III C, which focus on short, large, and intermediate containers, respectively. Representative values of Γ are selected in each section to illustrate the solutions; these selections are marked by vertical dotted lines in Fig. 3.

A. Small-aspect-ratio containers

Figure 4 shows three bifurcation diagrams (upper panels) in containers of heights (a) $H = 13.5$ mm ($\Gamma = 1.67$), (b) 10 mm ($\Gamma = 2.25$), and (c) 7.5 mm ($\Gamma = 3$); these values are marked by vertical lines in Fig. 3. The envelope of \widehat{T}_3 is plotted as a function of ΔT , for both increasing (black curve) and decreasing (thin gray curve) temperature. These diagrams are accompanied by the corresponding spectrograms (lower panels) showing the fast Fourier transforms (FFTs) of the signals as a function of ΔT . The frequency response is calculated over the range of ΔT where the oscillatory solutions are stable.

Figure 4(a) shows the details of the dynamics in the bistable region of the SW mode. Steady solutions correspond to $\widehat{T}_3 = 0$. By increasing the applied temperature gradient (following the solid curve) from the initial steady region, the envelope of \widehat{T}_3 is observed to suddenly increase to a finite value at $\Delta T \simeq 13.53$ K; recall that this is shifted with respect to the value calculated for $\varepsilon = 0$ in Sec. IID. This sharp jump is consistent with the subcritical character of the bifurcation since, when the steady solution becomes unstable, the system moves rapidly to the stable branch of finite-amplitude SWs created in the preceding saddle-node bifurcation (labeled SN_{SW}). The amplitude of the SWs along this branch increases with ΔT until achieving a maximum value near $\Delta T \simeq 23.30$ K. Beyond this, the SW amplitude decreases until the disappearance of this solution at $\Delta T \simeq 28.56$ K in the second saddle-node bifurcation. Above that, only steady flow solutions are found.

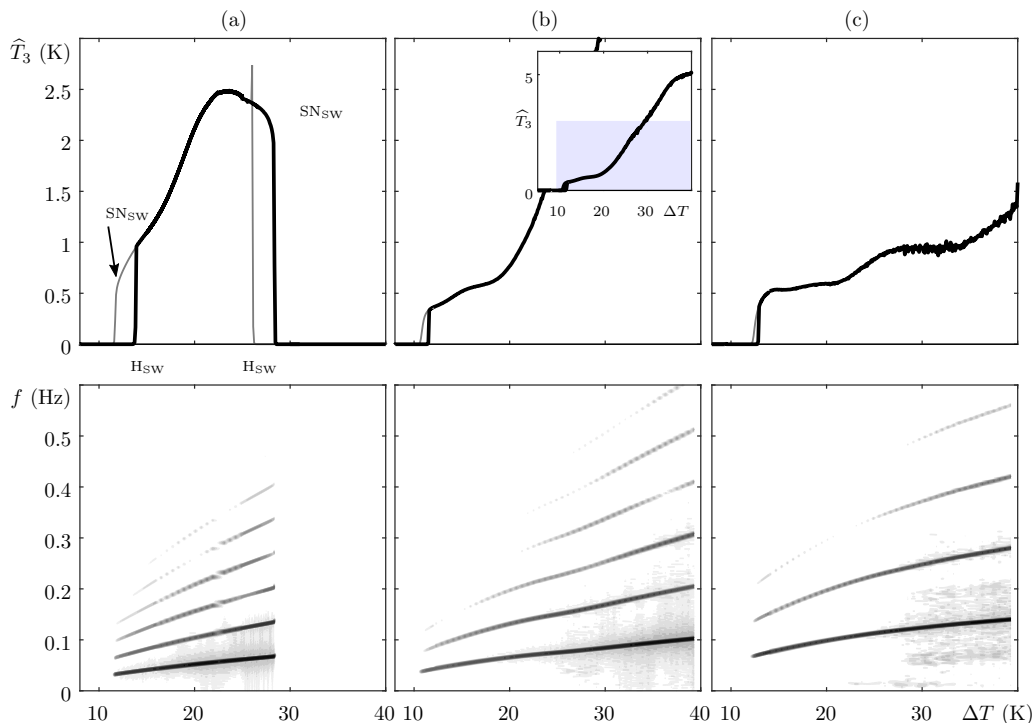


FIG. 4. Bifurcation diagrams (upper panels) showing the envelope of \hat{T}_3 vs ΔT in containers with (a) $H = 13.5$ mm ($\Gamma = 1.67$), (b) $H = 10$ mm ($\Gamma = 2.25$), (c) $H = 7.5$ mm ($\Gamma = 3$). Paths obtained by increasing (decreasing) ΔT are shown with black (thin gray) curves, with bifurcations labeled in (a). Spectrograms of \hat{T}_3 are shown in the lower panels, with the grayscale proportional to the logarithmic amplitude ratio (black indicating maximum amplitude).

When decreasing ΔT (following the thin gray curve in the figure) from the maximum value of 40 K, the stable steady flow at large ΔT becomes unstable at $\Delta T \simeq 26.41$ K via subcritical Hopf bifurcation. Again, this results in the sudden transition from the zero-amplitude (steady) solutions to a finite-amplitude branch of SWs—this stable branch connects in a saddle-node bifurcation at $\Delta T = 28.56$ K to the unstable branch of SW solutions created in the primary subcritical Hopf bifurcation. With continued reduction of ΔT , the SW amplitude first increases, then decreases, along the same path as before. In the case of gradual cooling, however, these periodic solutions persist below $\Delta T \simeq 13.53$ K, where the primary Hopf bifurcation was found, and only disappear when the saddle-node bifurcation at $\Delta T \simeq 11.45$ K is reached.

As seen in the associated spectrogram of \hat{T}_3 , the dominant frequency of the SW increases slightly from 0.03 to 0.06 Hz between the two saddle-node bifurcations; this dependence will be discussed further below. The spectrum is characterized by this dominant frequency and integer multiples of it.

The flow observed for this value of $H = 13.5$ mm ($\Gamma = 1.67$) is dominated by a large vortex whose center is shifted toward the hot lateral wall. For higher values of ΔT , a secondary vortex appears just below the free surface and close to the cold wall. This structure of two vortices constitutes the base flow upon which SWs appear. In Fig. 5 the temperature (colormap) and velocity fields (streamlines), averaged over one oscillation cycle, are illustrated for $\Delta T = 20$ K. Similar structures were found with short containers in the works of Carpenter and Homsy [15] and Peltier and Biringen [16].

The SW mode develops from the base flow state shown in Fig. 5. Figure 6 illustrates the SW solution found at $\Delta T = 20$ K ($Ma \simeq 1.24 \times 10^5$) through a series of eight snapshots of the

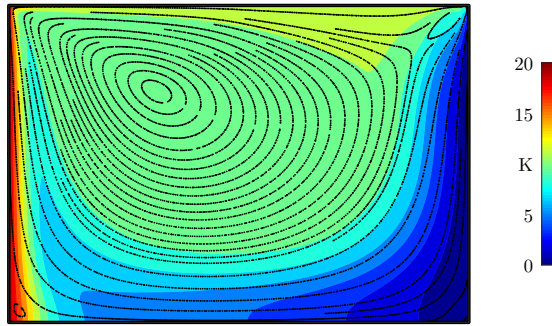


FIG. 5. Average temperature $\langle \delta T \rangle = \langle T - T_M \rangle$ and velocity $\langle \mathbf{u} \rangle$ illustrating the base flow of the SW mode for $H = 13.5$ mm ($\Gamma = 1.67$) and $\Delta T = 20$ K ($\text{Ma} \simeq 1.24 \times 10^5$).

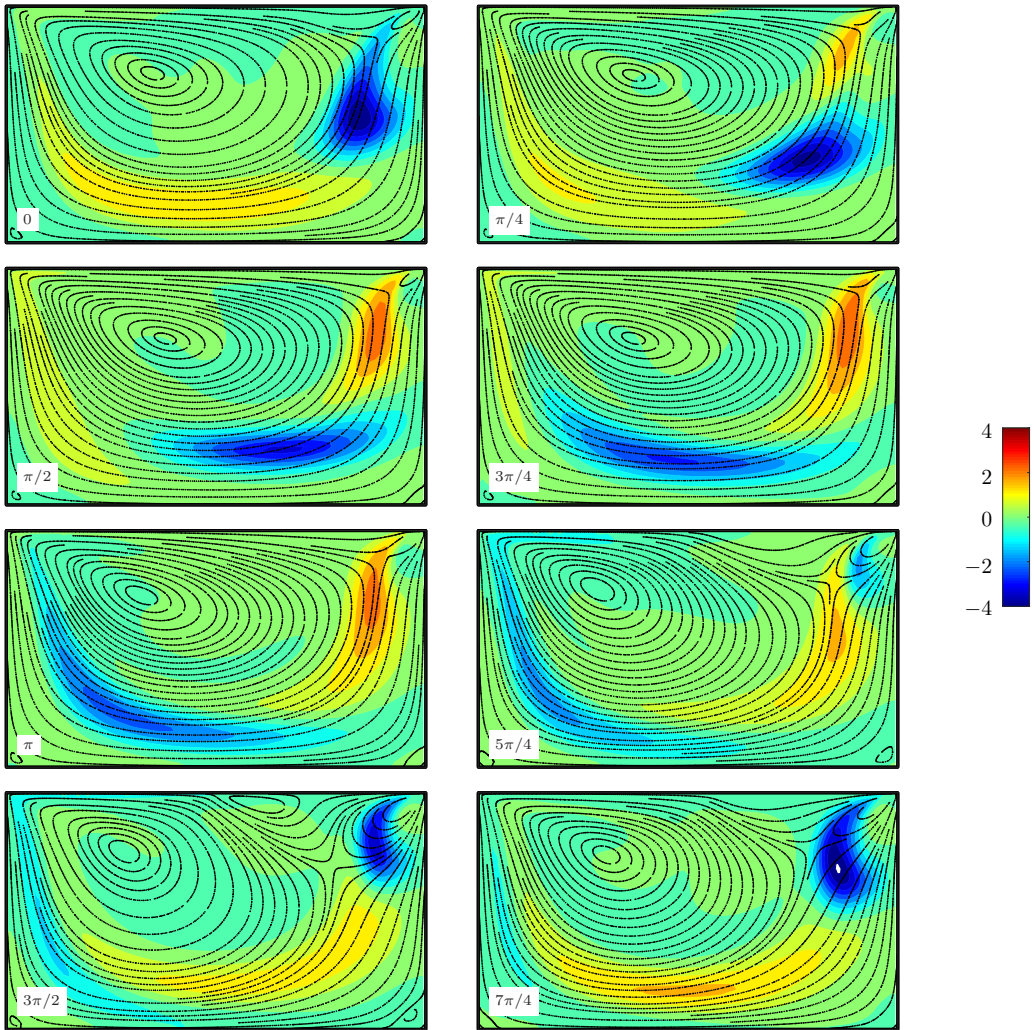


FIG. 6. Temperature deviation \hat{T} and instantaneous velocity field \mathbf{u} of the SW mode for $H = 13.5$ mm ($\Gamma = 1.67$) and $\Delta T = 20$ K ($\text{Ma} \simeq 1.24 \times 10^5$) at different phases of the oscillation cycle (labeled).

temperature deviation \hat{T} and the instantaneous velocity field \mathbf{u} . The snapshots are separated by one-eighth of the oscillation cycle (labeled by the corresponding phase in each panel).

The characteristics of the oscillation and the mechanism driving the instability can be understood following the description of Peltier and Biringen [16]. The largest vortex rotates in a clockwise sense, which propels a cool stream of liquid away from the cold wall and along the bottom of the container; see the snapshots in Fig. 6 between phases 0 and π . Near the hot wall, this stream is redirected upward, creating a cool tongue that interacts with the thermocapillary surface; see the snapshots at phases π and $5\pi/4$. The impact of the cool tongue on the surface establishes a large thermal gradient near the hot wall that causes the primary convection cell to compress and shift toward this boundary, becoming stronger in the process; these changes can be seen by comparing the evolution of the streamlines between phases π and $3\pi/2$. This compression reduces the shear force between this primary vortex and the secondary vortex with the same sense of rotation, allowing it to grow; it reaches its maximum strength at a phase of approximately $3\pi/2$. Between these main vortices, another (tertiary) vortex appears with the opposite sense of rotation, enabled by the shear between the primary and secondary cells and the weak local temperature gradient along that portion of the interface; see the snapshot at phase $3\pi/2$.

During the latter part of the cycle, the primary and secondary vortices strengthen up to a certain point, wherein two different mechanisms act to recover the initial structure. First, in the absence of sufficient reinforcement of liquid from the cold wall, the cool tongue near the hot wall warms and its effect on the surface diminishes; this retraction can be seen at phase $3\pi/2$ in the widening of the cold stream at the thermocapillary interface. Second, the increased strength of the primary vortex draws more warm liquid from the hot wall—note the warm tongue that is pulled up between phases π and $7\pi/4$. This process gradually extinguishes the secondary vortex cell while the primary vortex expands, restoring the original structure.

It is clear that this oscillation relies on an interaction between the sensitivity of the thermocapillary surface to the cooling effect provided by the cold tongue and the extent to which the cool stream emanating from the cold boundary can support this tongue. It stands to reason that the oscillation frequency would increase continuously with the driving force and the larger velocities associated with it, as observed in the spectrogram of Fig. 4(a).

To complete the analysis for $H = 13.5$ mm, we confirm the bistability of the system for $\Delta T \in (11.45, 13.53)$ K and $\Delta T \in (26.41, 28.56)$ K by taking two different paths to reach final temperatures within these intervals. Figures 7(a) and 7(b) show the time evolution of $\delta T_3 = T_3 - T_M$ for final ΔT values of (a) 12 K and (b) 28 K. In each case, two different profiles of ΔT are used to reach the final value (illustrated, respectively, with dark and light red lines) while maintaining the cold wall at a constant temperature $T = T_M$ (shown as a blue line).

One set of results in Fig. 7(a) is for a temperature difference ΔT that is raised linearly to 12 K and then maintained constant (dark red line). With this profile, the system does not undergo any primary instability because the H_{SW} curve is not crossed. This steady flow is reflected in the evolution of δT_3 (black curve) that first increases linearly then settles at a constant value of approximately 3 K. The final thermocapillary flow is steady.

The other set of results in Fig. 7(a) is obtained with a profile in which ΔT is increased up to a value of 15 K, beyond the primary bifurcation H_{SW} , then reduced again to the final value of 12 K (light red lines). With this profile, the steady flow becomes unstable to the SW mode during the final increase in ΔT , as revealed by the growth of oscillations in δT_3 (gray curve). Once SWs are triggered, reducing the applied ΔT to the final value of 12 K lowers the oscillation amplitude but does not restore the steady flow, consistent with the diagram of Fig. 4(a). The final thermocapillary flow in this case is oscillatory, which confirms bistability (as opposed to merely a delay effect) and the existence of the saddle-node bifurcation in the subcritical region that creates it.

Analogous sets of results in Fig. 7(b) confirm the bistability of the higher temperature transition region. In one case, ΔT is raised past the (upper branch of the) critical curve H_{SW} until reaching the final value of 28 K. Since the Hopf bifurcation is subcritical and SN_{SW} lies above the final

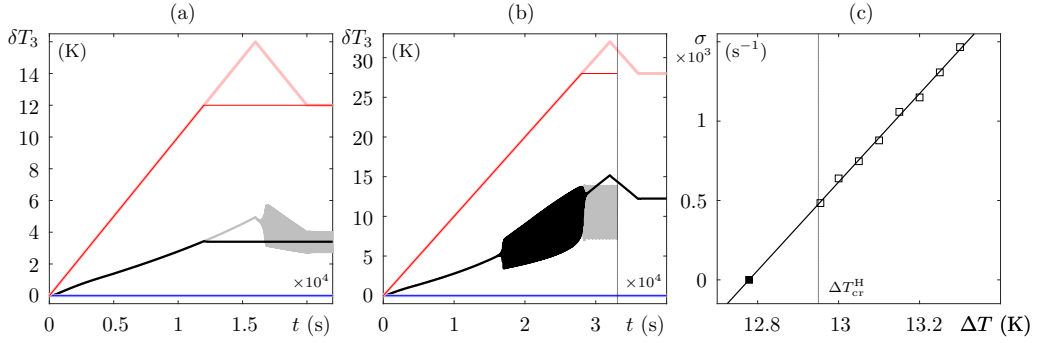


FIG. 7. [(a), (b)] Temporal evolution of δT_3 in a container of $H = 13.5$ mm ($\Gamma = 1.67$) for ΔT between the Hopf and saddle-node bifurcations: (a) bistable solutions at $\Delta T = 12$ K, near the first critical temperature; (b) bistable solutions at $\Delta T = 28$ K, near the second critical temperature. In both panels, the black (gray) line shows the instantaneous value of δT_3 with the applied ΔT profile shown with dark (light) red lines. The constant temperature T_M of the right boundary is indicated with a blue line. (c) The measured (open squares) exponential growth rate σ as a function of ΔT near the primary Hopf bifurcation. A linear fit indicates a threshold near 12.78 K while the value of $\Delta T_{cr}^H = 12.95$ K found in Sec. IID is indicated with a vertical line.

temperature, the SWs do not lose stability but persist in the final state, as seen in the oscillations of δT_3 (gray curve in the figure). By using a different profile that raises ΔT beyond the SN_{SW} curve to 32 K, a transition to steady flow is triggered. This steady flow (black curve) remains even as ΔT is lowered again to 28 K.

The bistable nature of the primary Hopf bifurcation shown in Fig. 7(a) is further confirmed by measurements of its exponential growth rate σ (open markers) as a function of the applied ΔT in Fig. 7(c). Numerical measurements (open markers) are then fitted with a linear function to estimate the critical value (solid marker). While this value of $\Delta T \simeq 12.78$ K lies slightly below the value of $\Delta T_{cr}^H = 12.95$ K obtained in Sec. IID, it is close enough to reinforce the conclusion of bistability.

This picture of pattern selection in small containers is complemented with the results for two additional container heights of 10 and 7.5 mm, which were shown, respectively, in Figs. 4(b) and 4(c); see also the vertical dotted lines in Fig. 3. The bifurcation diagrams and associated spectrograms reveal a simpler scenario in those containers. As ΔT is increased with $H = 10$ mm ($H = 7.5$ mm) the flow undergoes a subcritical Hopf bifurcation to the SW mode at $\Delta T \simeq 11.34$ K ($\Delta T \simeq 12.72$ K), with the corresponding saddle-node bifurcation occurring at $\Delta T \simeq 10.42$ K ($\Delta T \simeq 11.99$ K). The unstable SW solution branch created in this Hopf bifurcation is stabilized by the saddle node, which creates a small region of bistability. The SWs remain stable as ΔT is raised further (over the range of parameters explored). As with $H = 13.5$ mm, these SW are characterized by a single dominant frequency that increases continuously with ΔT (i.e., with the driving force). The frequency is somewhat higher in these cases compared to that of $H = 13.5$ mm, which can be partly explained by looking at the scale of the vortical structure in the base flow. It is worth noting that for $H = 7.5$ mm [Fig. 4(c)], the envelope of \hat{T}_3 shows irregular variations at higher ΔT values, which may be indicative of a transition to chaotic flow, something not investigated here.

To better compare the differences in the SW mode for different heights, Fig. 8 illustrates the base flow for $H = 7.5$ mm, while Fig. 9 shows a series of snapshots during one cycle of the SW oscillation. It is evident that reducing the container height limits the size of the large vortex near the hot side, whose scale is set by H . This reduction allows the vortex near the cold side to grow and occupy a larger portion of the container. As H is lowered further, this secondary vortex extends enough to leave room for a third vortex to appear in the vicinity of the thermocapillary interface near the cold wall.

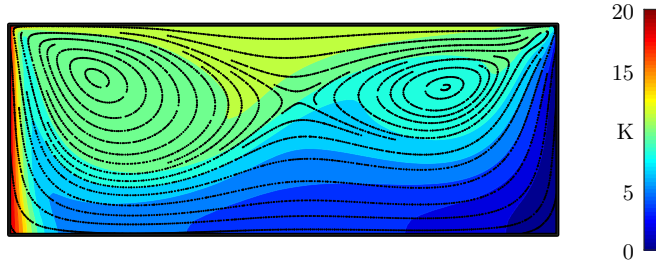


FIG. 8. Average temperature distribution $\langle \delta T \rangle$ and velocity field $\langle \mathbf{u} \rangle$ illustrating the base flow of the SW mode for $H = 7.5$ mm ($\Gamma = 3$) and $\Delta T = 20$ K ($\text{Ma} \simeq 1.24 \times 10^5$).

The SW mode develops from the base flow structure illustrated in Fig. 8 and, due to the shared instability mechanism, has features like those seen with $H = 13.5$ mm. The details of the oscillation cycle are captured by eight equally spaced snapshots in Fig. 9 that show the temperature deviation \hat{T} and the instantaneous velocity \mathbf{u} . Again, the oscillation is supported by the interaction between cool tongues siphoned off the cold wall and the thermocapillary interface near the hot wall. This modulates the strength of the large vortex near the hot wall, which retracts and expands during the oscillation cycle, and leads to the appearance and subsequent disappearance of an oppositely rotating auxiliary vortex near the interface; see the snapshot at phase $3\pi/2$. The expansion is later driven by the arrival of a warm tongue of liquid to the hot wall, which acts to reduce the local thermal gradient.

Compared to the case of $H = 13.5$ mm shown Fig. 6, the time needed for a warm/cool tongue (temperature perturbation) to reach the hot boundary is reduced. This can be attributed, in part, to the smaller size of the vortices and, in particular, the vortex near the hot wall, which plays a key role in transporting SW perturbations. The contraction of this vortex as Γ increases is associated with an increase in the oscillation frequency; see the spectrograms of Fig. 4.

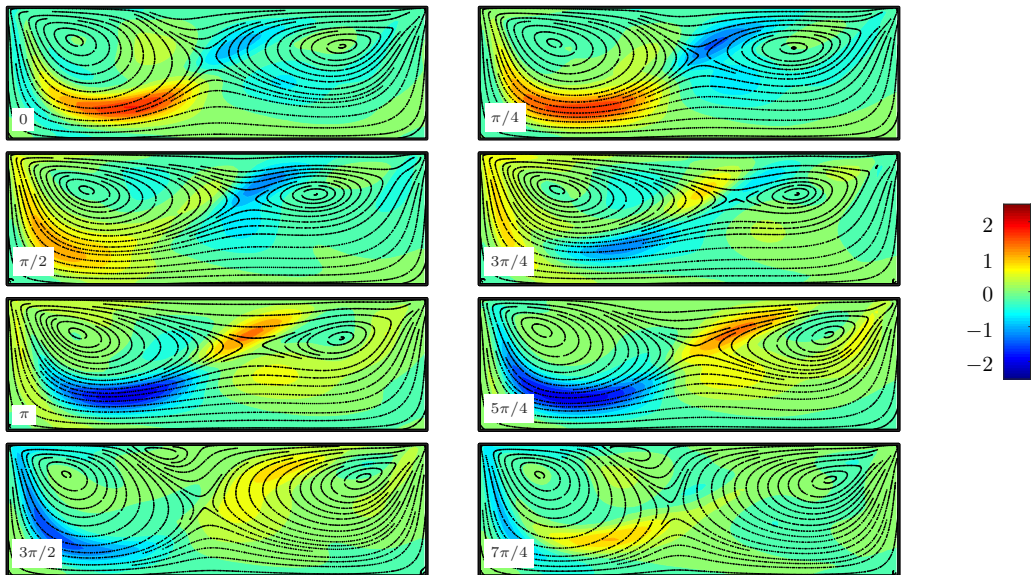


FIG. 9. Temperature deviation \hat{T} and instantaneous velocity \mathbf{u} for the SW mode with $H = 7.5$ mm ($\Gamma = 3$) and $\Delta T = 20$ K ($\text{Ma} \simeq 1.24 \times 10^5$) at different phases of the oscillation cycle (labeled).

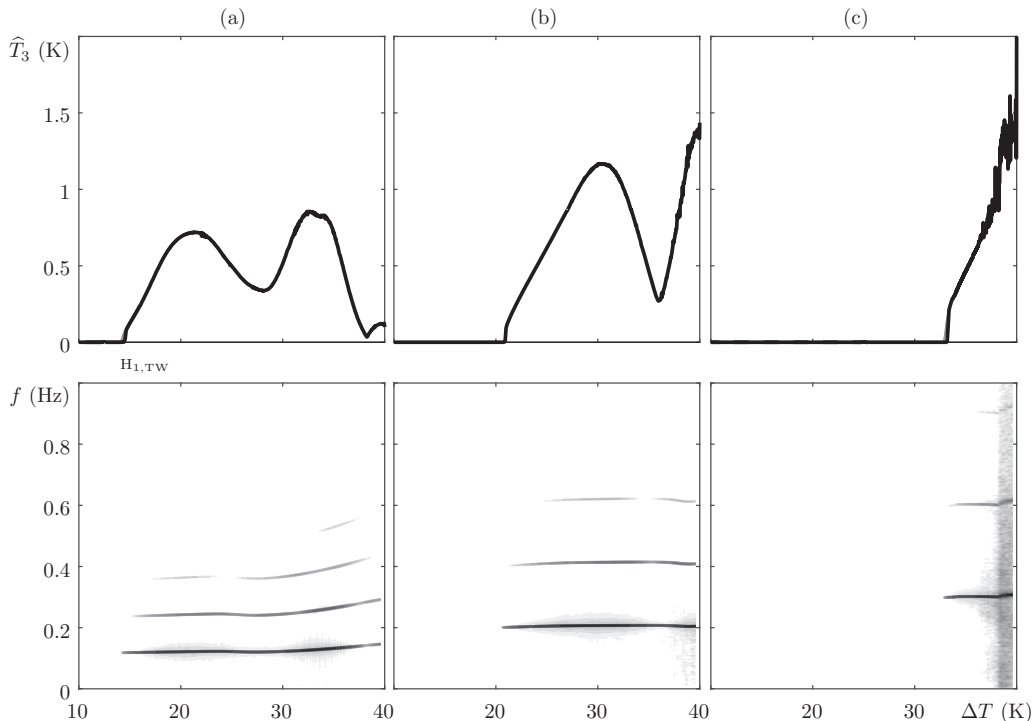


FIG. 10. Bifurcation diagrams (upper panels) showing the envelope of \widehat{T}_3 as a function of ΔT and associated spectrograms (lower panels), again with the grayscale proportional to the logarithmic amplitude ratio, obtained for containers of (a) $H = 2.5$ mm ($\Gamma = 9$), (b) $H = 1.875$ mm ($\Gamma = 12$), and (c) $H = 1.5$ mm ($\Gamma = 15$). Results for increasing (decreasing) ΔT are shown with black (thin gray) curves; these are nearly indistinguishable in the plots.

B. Large-aspect-ratio containers

Figure 10 presents three bifurcation diagrams (upper panels) showing the envelope of \widehat{T}_3 as a function of ΔT , obtained for containers of (a) $H = 2.5$ mm ($\Gamma = 9$), (b) $H = 1.875$ mm ($\Gamma = 12$), (c) $H = 1.5$ mm ($\Gamma = 15$); these values are marked by vertical dotted lines in Fig. 3. Results are included for both increasing and decreasing ΔT , indicated by black and thin gray curves, respectively; these are nearly indistinguishable on the scale of the figure. The diagrams are accompanied in the lower panels by spectrograms of \widehat{T}_3 .

The bifurcation diagrams have a somewhat similar shape, differing mainly in the delay of the primary Hopf bifurcation with smaller H (larger Γ). The initial region of steady thermocapillary flow, which corresponds to $\widehat{T}_3 = 0$, becomes unstable to the TW mode as $H_{1,TW}$ is surpassed at $\Delta T \simeq 14.36$ K, 20.74 K and 33.06 K, respectively. For this range of Γ , the primary Hopf bifurcation is supercritical and associated with the gradual growth of the oscillation amplitude above onset. Supercriticality is confirmed by simulations with decreasing ΔT , which provide estimates of the onset that differ by less than 0.25 K from the above values. This delay is attributed to the use of $\varepsilon = 10^{-4}$ K/s, as discussed in Sec. II D.

The three spectrograms reveal a dominant frequency that is largely independent of the applied ΔT , with values of 0.12, 0.20, and 0.30 Hz, respectively. The case of $H = 2.5$ mm [Fig. 10(a)], however, does exhibit a slight increase in the oscillation frequency at large ΔT . In contrast to the mild variation with ΔT , we observe an approximate linear dependence of the initial Hopf frequency on Γ : $\omega_H/(2\pi) = (0.03\Gamma - 0.17)$ Hz. These aspects of the spectrograms will be discussed below.

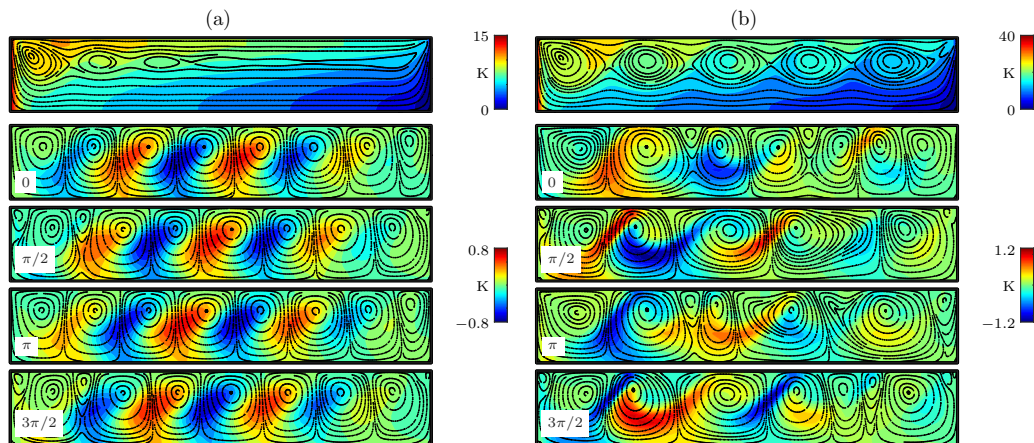


FIG. 11. The TW mode with (a) $\Delta T = 15$ K ($\text{Ma} \simeq 9.31 \times 10^4$) and (b) $\Delta T = 40$ K ($\text{Ma} \simeq 2.48 \times 10^5$) in a container of $H = 2.5$ mm ($\Gamma = 9$). The upper panels show the average (base) temperature $\langle \delta T \rangle$ and velocity $\langle \mathbf{u} \rangle$. The lower panels show snapshots of the instantaneous temperature \hat{T} and velocity $\hat{\mathbf{u}} = \mathbf{u} - \langle \mathbf{u} \rangle$ deviations over one oscillation period.

Finally, we note the appearance of irregular variations in the envelope of \hat{T}_3 at large ΔT in Fig. 10(c) and less so in Fig. 10(b), which are also reflected in the spectrogram. This behavior suggests a transition to chaotic flow, which has been investigated in rectangular liquid layers by several numerical studies, identifying, in particular, the Ruelle-Takens-Newhouse route to chaos [67,68]. These analyses were recently extended by Li *et al.* [69] in an effort to explore the effect of geometry and Pr. They conducted a numerical analysis of the behavior of 10 cSt silicone oil for $\Gamma = 13, 14.25$. One can conclude from the results that the finite extent of the layer has a significant influence on the spatiotemporal evolution of the flow and on the selected route to chaos. For $\Gamma = 13$, the route to chaos was associated with a cascade of periodic-doubling bifurcations, while for $\Gamma = 14.25$, the appearance of chaos was preceded by a quasiperiodic state with frequency locking.

The flow observed with $H = 2.5$ mm ($\Gamma = 9$) is shown in Fig. 11 for (a) $\Delta T = 15$ K ($\text{Ma} \simeq 9.31 \times 10^4$) and (b) $\Delta T = 40$ K ($\text{Ma} \simeq 2.48 \times 10^5$). The upper panel shows the average (base) flow, while the four lower panels show equally spaced snapshots of the temperature \hat{T} and velocity $\hat{\mathbf{u}}$ deviations from this base flow during one period of the oscillation,

For $\Delta T = 15$ K, the structure of the base flow is characterized by a series of vortices that spread inward from the hot wall, with their centers aligned at approximately $2/3$ of the container height. This type of flow was referred to as a *steady multicellular structure* (SMC) by Shevtsova *et al.* [25], who analyzed thermocapillary-driven flows in a large container with $\Gamma = 24.7$ under different dynamic Bond numbers. The intensity of the vortices within the SMC structure decays exponentially with distance from the hot wall. The TW mode that develops from this base flow is characterized by the cyclic creation of vortices near the cold wall that detach and move toward the hot wall. The motion of these traveling waves can be seen by comparing the different phases included in Fig. 11(a), from which the leftward movement of the warm/cool perturbations separating traveling vortices is clear. Starting from the cold wall, it is also apparent that these perturbations grow in amplitude near the center of the container and diminish again as they approach the hot wall. These results are consistent with the observations of Shevtsova *et al.* [25].

After increasing ΔT from 15 to 40 K, clear differences arise, both in the base flow and in the oscillations; see Fig. 11(b). First, the increased thermocapillary force results in a SMC state that extends throughout the container with all vortices of comparable intensity and with a characteristic size set by H . It is apparent from a comparison of the two cases that increasing ΔT increases the strength and extent of the SMC state. At some point, its extent is limited by the cold wall and further

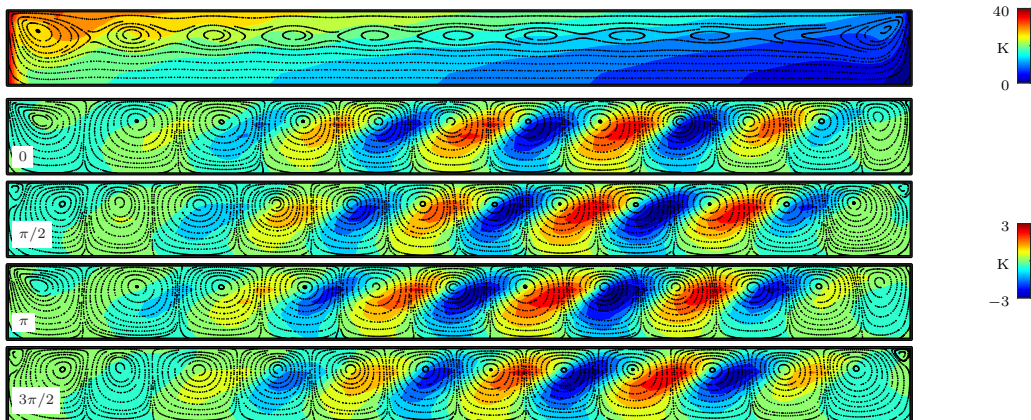


FIG. 12. The TW mode with $\Delta T = 40$ K ($\text{Ma} \simeq 2.48 \times 10^5$) in a container of $H = 1.5$ mm ($\Gamma = 15$). The upper panel shows the average (base) temperature $\langle \delta T \rangle$ and velocity $\langle \mathbf{u} \rangle$. The lower panels show snapshots of the instantaneous temperature \hat{T} and velocity $\hat{\mathbf{u}}$ deviations over one oscillation period.

increases in the strength of the thermocapillary force are reflected in the overall amplification of vortex intensity. This is consistent with the importance of finite-size effects pointed out by Li *et al.* [69].

From this base state TWs develop, but with more complicated dynamics than in the case of $\Delta T = 15$ K. While thermal perturbations (and associated vortices) clearly travel from the cold to the hot wall, these perturbations are pulled and deformed by the base flow; note the curvature of the cool and warm tongues in Fig. 11(b) as they are rotated by the vortices of the underlying flow. This behavior helps explain the dependence of the TW frequency on ΔT that can be observed in the spectrogram of Fig. 10(a) at large values. An increase in the driving force means that the perturbations travel faster around the vortices of the base flow, which increases the frequency of the TW oscillations.

The effect of reducing the container height is illustrated in Fig. 12, which shows the flow obtained with $H = 1.5$ mm ($\Gamma = 15$) and $\Delta T = 40$ K ($\text{Ma} \simeq 2.48 \times 10^5$). The upper panel shows the average (base) flow, while the lower panels contain snapshots of the temperature and velocity deviations from this base flow at different phases of the oscillation cycle. The structure of the base flow is again characterized by a large SMC state. Compared to the case of Fig. 11(b) with $\Gamma = 9$ at the same ΔT , there are twice as many (ten) vortices distributed along the container length. The intensity of these vortices decays (exponentially) with distance from the hot wall [25], except in the vicinity of the cold wall where the high temperature gradient near the interface strengthens the rightmost vortex. The characteristics of the oscillation cycle, illustrated in the lower panels, are analogous to those described with Fig. 11(a).

C. Intermediate-aspect-ratio containers

Finally, we analyze the regime of intermediate Γ ; the shaded blue region in the stability map of Fig. 3. Figure 13 shows three bifurcation diagrams (upper row of panels) in containers of (a) $H = 5$ mm ($\Gamma = 4.5$), (b) $H = 3.5$ mm ($\Gamma = 6.42$), (c) $H = 3$ mm ($\Gamma = 7.5$); these values are marked by dotted vertical lines in Fig. 3. The envelope of \hat{T}_3 is plotted as a function of ΔT and results are included for both heating and cooling ramps, rendered as black and thin gray curves, respectively; these are nearly indistinguishable in the plots. The diagrams are accompanied by spectrograms to show the dependence of the dominant frequency on ΔT .

The results for $H = 5$ mm in Fig. 13(a) are representative of containers with $4 \lesssim \Gamma \lesssim 6$, where both TW and SW modes can be excited depending on ΔT . Upon increasing the applied temperature

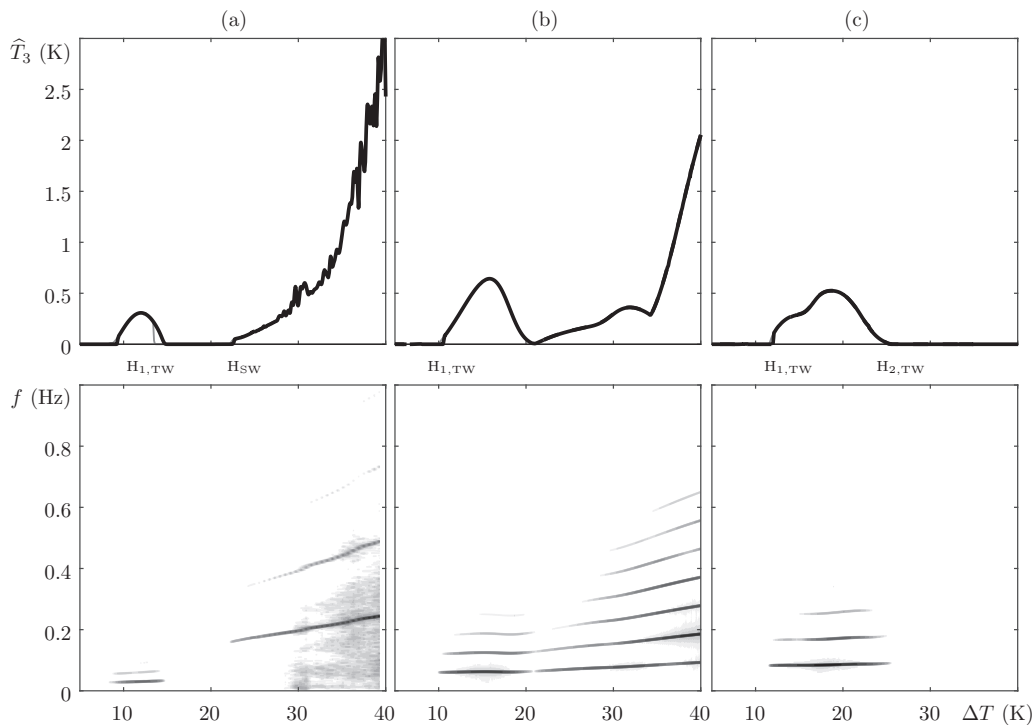


FIG. 13. Bifurcation diagrams (upper panels) showing the envelope of \hat{T}_3 as a function of ΔT and associated spectrograms (lower panels), again with the grayscale proportional to the logarithmic amplitude ratio, for containers of (a) $H = 5$ mm ($\Gamma = 4.5$), (b) $H = 3.5$ mm ($\Gamma = 6.42$), (c) $H = 3$ mm ($\Gamma = 7.5$). Results for increasing (decreasing) \hat{T}_3 are shown with black (thin gray) curves; they are nearly indistinguishable in most regions.

difference, the initial steady thermocapillary flow first loses stability to the TW mode as the lower branch of the $H_{1,TW}$ curve is crossed at $\Delta T \simeq 9.14$ K. These TWs are found within a narrow region of ΔT limited by the upper branch of the $SN_{1,TW}$ curve at $\Delta T \simeq 14.99$ K. Beyond this value, the flow becomes steady again and remains so over a relatively large interval of ΔT (the central portion of the plot where $\hat{T}_3 = 0$). With further increase in ΔT , this steady flow loses stability to the SW mode via a supercritical Hopf bifurcation at $\Delta T \simeq 20.40$ K. The supercriticality of this SW instability is reflected in the gradual growth of $\hat{T}_3 = 0$ near onset. Increasing the applied temperature gradient even more does not change the nature of the selected mode but does lead to the appearance of irregular variations in the signal of \hat{T}_3 , suggesting a transition to chaotic dynamics [69]; this behavior is also reflected in the spectrogram. Decreasing ΔT from the region of stable SWs confirms the subcritical nature of $H_{1,TW}$, which is accompanied by the saddle node $SN_{1,TW}$ that sets the width of the bistable region, as in Sec. III A.

The results for $H = 3.5$ mm, presented in Fig. 13(b), show that the stable TWs created in the initial Hopf bifurcation persist for larger ΔT , at least within the explored interval of parameters. One can observe, however, a change in behavior at $\Delta T \approx 20$ K where the frequency of the TW oscillations begins to increase slightly with ΔT ; prior to that, it is nearly constant. Such behavior was discussed in Sec. III B and can be attributed to the increasing strength of the base flow, which carries the perturbations with greater velocity.

The case of $H = 3$ mm is shown in Fig. 13(c). The subcritical bifurcations $H_{1,TW}$ and $H_{2,TW}$ coexist for this aspect ratio, which limits the region of stable TWs to an interval of moderate ΔT values. Steady flow is found for the explored range of ΔT beyond this.

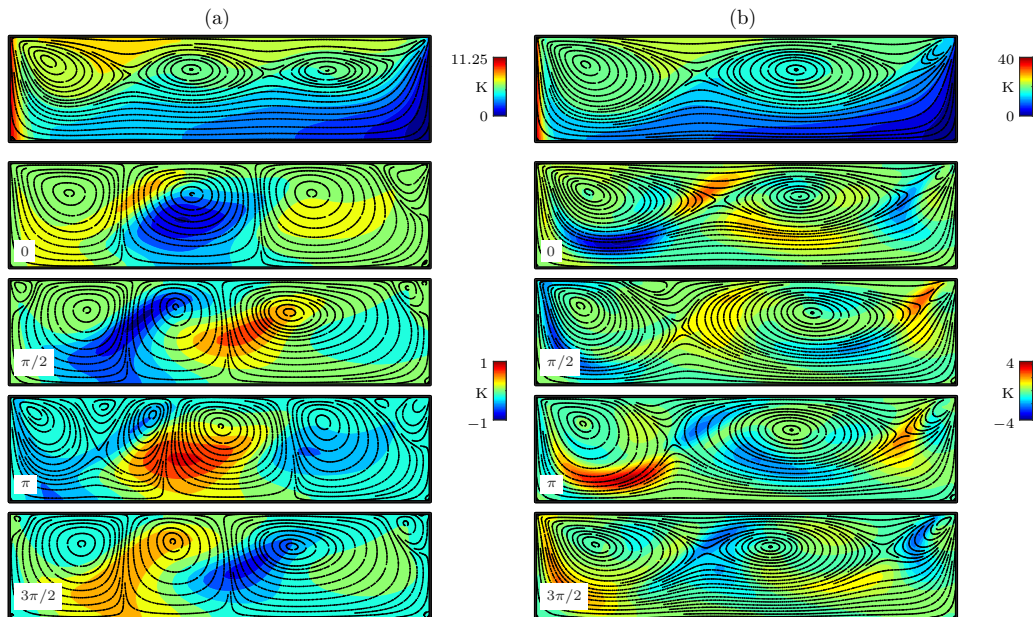


FIG. 14. Dynamics of the TW and SW modes, respectively, at (a) $\Delta T = 11.25$ K ($\text{Ma} \simeq 6.98 \times 10^4$), (b) $\Delta T = 40$ K ($\text{Ma} \simeq 2.48 \times 10^5$) in a container of $H = 5$ mm ($\Gamma = 4.5$). The upper panels show the average (base) temperature (δT) and velocity (\mathbf{u}) of the solution. The lower panels show the deviations \hat{T} and $\hat{\mathbf{u}}$ over one cycle.

The dynamics of the flow for intermediate-aspect-ratio containers is illustrated in Fig. 14 for $H = 5$ mm, where both TWs and SWs can be found. The TW mode at $\Delta T = 11.25$ K ($\text{Ma} \simeq 6.98 \times 10^4$) is depicted in Fig. 14(a), which shows the average (base) flow in the upper panel and the deviations \hat{T} and $\hat{\mathbf{u}}$ at equally spaced moments of the oscillation cycle in the lower panels. The SW mode at $\Delta T = 40$ K ($\text{Ma} \simeq 2.48 \times 10^5$) is illustrated in the same manner in Fig. 14(b).

Compared to the large-aspect-ratio case of Sec. III B, the characteristics of the TW mode are a bit different. There are substantially fewer vortices in the base flow and, thus, the finite size of the container is expected to play a more significant role. This is evident from the equally spaced snapshots of the perturbation fields \hat{T} and $\hat{\mathbf{u}}$, which show structures on the same length scale as the container. In contrast to Fig. 12, where the vortical perturbations have nearly constant length (size) and are regularly spaced across the container, the size of the TW vortices in Fig. 14(a) varies in both space and time. The dynamics of the SW mode, on the other hand, are analogous to those described in Sec. III A, with the same type of back-and-forth pulsation of the vortical structure. It is also apparent in Fig. 14(b) how the cool tongue acts to compress the large vortex near the hot wall and allow the creation of a smaller tertiary vortex near the free surface; see the snapshot at $\pi/2$.

IV. APPLICATION TO PHASE CHANGE DYNAMICS IN MICROGRAVITY

We now apply the results of Sec. III to the recent investigation by Salgado Sánchez *et al.* [26] of pattern selection in thermocapillary flows during melting in microgravity. For completeness, we describe in Sec. IV A the mathematical formulation used to resolve the phase change dynamics. The stability limits obtained during the phase change process are then compared in Sec. IV B to the stability map of Sec. III. Finally, the transitions observed during melting are explained in terms of the effective Ma and Γ in both small, large and intermediate containers in Secs. IV C, IV D, and IV E, respectively.

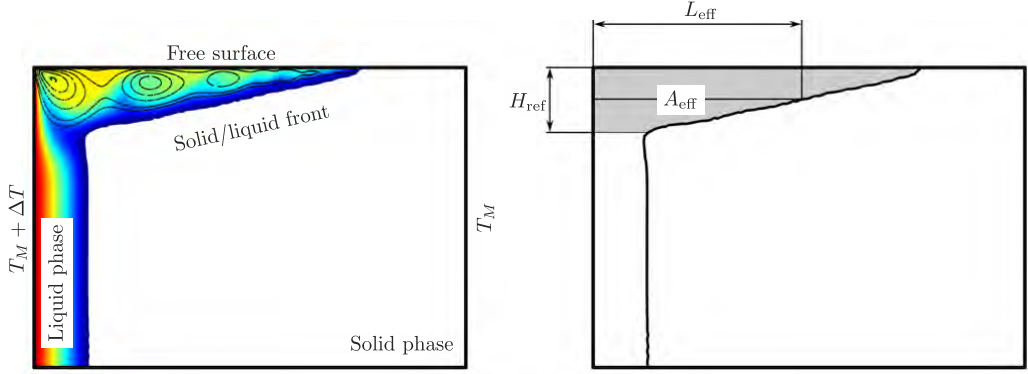


FIG. 15. (Left) Sketch showing the system treated by the numerical model used to resolve the phase change: an open rectangular container of n -octadecane melted by applying constant temperatures $T_M + \Delta T$ and T_M along opposite lateral walls. (Right) Calculation of the effective aspect ratio $\Gamma_{\text{eff}} = L_{\text{eff}}/H_{\text{ref}}$ during melting.

A. Statement of the problem

The melting of an open rectangular volume of n -octadecane in microgravity is considered, driven by constant temperatures on the opposing lateral walls. The process naturally generates thermal gradients that modify the surface tension of the melted liquid, which generates thermocapillary convection. A sketch of the setup considered in the numerical model is provided in Fig. 15(a).

As in Sec. II, the flow in the liquid phase is considered laminar and incompressible and the conservation of mass and momentum is described by Eqs. (1a) and (1b). Following the enthalpy method for convection/diffusion phase change proposed by Voller *et al.* [70], the conservation of thermal energy is modified here to include the contribution of the heat of fusion c_L :

$$\rho c_p \left(\frac{\partial T}{\partial t} + \mathbf{u} \cdot \nabla T \right) = \nabla \cdot (k \nabla T) - \rho c_L \left(\frac{\partial f}{\partial t} + \mathbf{u} \cdot \nabla f \right). \quad (12)$$

During melting, the amount of heat absorbed depends on the fraction of melted material f through the product $f \rho c_L$. Thermal energy and momentum are thus coupled through f , which can be expressed as a field depending on temperature as

$$f(\tilde{T}) = \begin{cases} 0 & \tilde{T} < -1/2, \\ \frac{1}{2} + \tilde{T} + \frac{1}{2\pi} \sin 2\pi \tilde{T} & |\tilde{T}| \leq 1/2, \\ 1 & \tilde{T} > 1/2, \end{cases} \quad (13)$$

where $\tilde{T} = (T - T_M)/\delta_T$. Note that f changes (symmetrically) from 0 to 1 near T_M . The small temperature δ_T characterizes the width of the so-called *mushy region* [71] where solid and liquid phases can coexist.

The melting material is modelled as a single phase with physical properties that depend on T and have appropriate limits for the solid and liquid phases. These are written using the liquid fraction f as follows:

$$\rho = \rho_S + (\rho_L - \rho_S)f, \quad (14a)$$

$$\mu = \mu_S + (\mu_L - \mu_S)f, \quad (14b)$$

$$c_p = c_{pS} + (c_{pL} - c_{pS})f, \quad (14c)$$

$$k = k_S + (k_L - k_S)f, \quad (14d)$$

TABLE III. Latent heat and relevant physical properties of solid n -octadecane, reproduced from Ref. [31].

Latent heat, c_L	243.5 kJ/kg
Density, ρ	865 kg/m ³
Heat capacity at constant pressure, c_p	1934 J/(kg K)
Thermal conductivity, k	0.358 W/(m K)

where the subscripts L and S denote liquid and solid, respectively. The parameter μ_S is a virtual solid viscosity several orders of magnitude greater than μ_L [70] to ensure that the velocity in the solid is effectively zero.

The boundary conditions, including those describing the thermocapillary effect, are as in Sec. II with the additional condition that $\gamma = 0$ if $T \leq T_M$ along the open boundary.

Again, we use L , (L^2/α) and ΔT to rescale length, time, and temperature, and take the physical properties of the liquid phase as reference values. In addition to the dimensionless parameters of Sec. II, the dynamics of the phase change depends on the Stefan number

$$\text{Ste} = \frac{c_{pL}\Delta T}{c_L}, \quad (15)$$

and on the ratios between the physical properties in each phase

$$\tilde{\rho} = \frac{\rho_S}{\rho_L}, \quad \tilde{\mu} = \frac{\mu_S}{\mu_L}, \quad \tilde{c}_p = \frac{c_{pS}}{c_{pL}}, \quad \tilde{k} = \frac{k_S}{k_L}. \quad (16)$$

The additional properties of the solid phase are provided in Table III, from which we obtain the ratios $\tilde{\rho} = 1.11$, $\tilde{k} = 2.42$, $\tilde{c}_p = 0.88$.

As above, COMSOL Multiphysics is used to solve the problem in dimensional variables with an analogous numerical scheme. The initial condition for T is 25 °C ($< T_M$) at which the material is solid and $\mathbf{u} = 0$. The maximum mesh size is selected as in Sec. II, and the remaining numerical parameters are set to $\delta_T = 1$ K and $\mu_S = 10^3$ Pa s. This choice of parameters was validated against experiments by Salgado Sánchez *et al.* [31]. That work considered a fixed rectangular geometry, neglected the small volume changes between solid and liquid phases during melting, and demonstrated good agreement between experimental results and simulations. Additional details of the numerical method, including convergence tests and the criteria used for selecting the maximum mesh size, δ_T and μ_S , can be found in Refs. [26,31,32].

Until melting is completed, the solid/liquid front constitutes a *dynamic boundary condition* for the liquid phase. The shape of this front often reflects two distinct regions: one dominated by conduction, where the isotherms are nearly parallel to the hot wall, and one dominated by the thermocapillary effect near the thermocapillary interface [26]. For this latter region, in particular, the progression of the solid/liquid front changes both its length and depth. Time-dependent effective values of Γ and Ma may then be used to characterize the region of liquid dominated by thermocapillary flow. In order to compare the patterns and dynamics described by Salgado Sánchez *et al.* [26] during melting with those of Sec. III, we define the effective parameters in the following manner.

The region dominated by thermocapillary flow can be characterized by the ‘‘corner’’ point where the solid/liquid front changes from nearly vertical to sloping; see Fig. 15. Specifically, we define this point as the one on the solid/liquid front closest to the upper left corner of the container. The distance from this point to the top of the container is the reference height H_{ref} . Note that this definition makes sense even in the large-aspect-ratio limit, where the thermocapillary layer extends across the full height of the container.

TABLE IV. Summary of the melting processes analyzed, showing key parameters and observed flow regimes (and transitions).

Melting no.	Γ	H (mm)	Ma	ΔT (K)	Flow regime(s)
1	2.25	10	6.21×10^4	10	S
2	2.25	10	1.86×10^5	30	S \rightarrow SW
3	1.5	15	2.48×10^5	40	S \rightarrow SW \rightarrow S
4	12	1.875	7.76×10^4	12.5	S
5	12	1.875	1.86×10^5	30	S \rightarrow TW
6	5.29	4.25	7.76×10^4	12.5	S \rightarrow TW
7	5.29	4.25	1.29×10^5	20.75	S
8	5.29	4.25	1.40×10^5	22.5	S \rightarrow SW

After determining H_{ref} at given a time of the melting, the liquid area within the thermocapillary layer is calculated from

$$A_{\text{eff}} = \int_{H_{\text{ref}}}^H dA \quad (\text{liquid}; T > T_M). \quad (17)$$

The effective length L_{eff} is then defined from the position of the solid/liquid front along a horizontal line located a distance $H_{\text{ref}}/2$ below the thermocapillary interface. The effective height is obtained from $H_{\text{eff}} = A_{\text{eff}}/L_{\text{eff}}$. These dimensions together define an ‘‘equivalent’’ rectangular container with effective aspect ratio

$$\Gamma_{\text{eff}} = \frac{L_{\text{eff}}}{H_{\text{eff}}}, \quad (18)$$

and Ma:

$$\text{Ma}_{\text{eff}} = \frac{\gamma L_{\text{eff}} \Delta T}{\mu_L \alpha}. \quad (19)$$

These definitions are used below to analyze the melting process in terms of the path it describes in the parameter space of $(\Gamma_{\text{eff}}, \text{Ma}_{\text{eff}})$.

Table IV summarizes the selection of representative melting processes analyzed below, including the relevant parameters and flow regimes (transitions) observed. With the exception of no. 3, these are adapted from Ref. [26]. For the sake of generality, most of the results discussed below are presented in dimensionless variables, but are accompanied by dimensional values in parentheses to facilitate physical interpretation and comparison with experiments.

B. Dynamics of melting in microgravity

We briefly review the dynamics of thermocapillary flow observed during the melting of n -octadecane in microgravity, with more detailed results available in Ref. [26].

In large Γ containers, the thermocapillary flow at low Ma is initially characterized by a steady return flow (SRF) solution [17,18]. Increasing Ma destabilizes this SRF solution to a SMC state. Still further increase in Ma induces a transition to periodic TWs with the characteristic creation of vortices at the cold side.

In small Γ containers, the thermocapillary flow at small-to-moderate Ma initially features a transition from a small-scale SMC located near the open boundary of the container to a large-scale steady vortical structure. Upon increasing Ma, a complex oscillatory mode appears, characterized by pulsation of the underlying vortical structure. Its structure evolves as the solid/liquid front advances, with a reduction in the number of vortices and the frequency of oscillation. This mode was classified as a SW due to its qualitative differences with the TW mode.

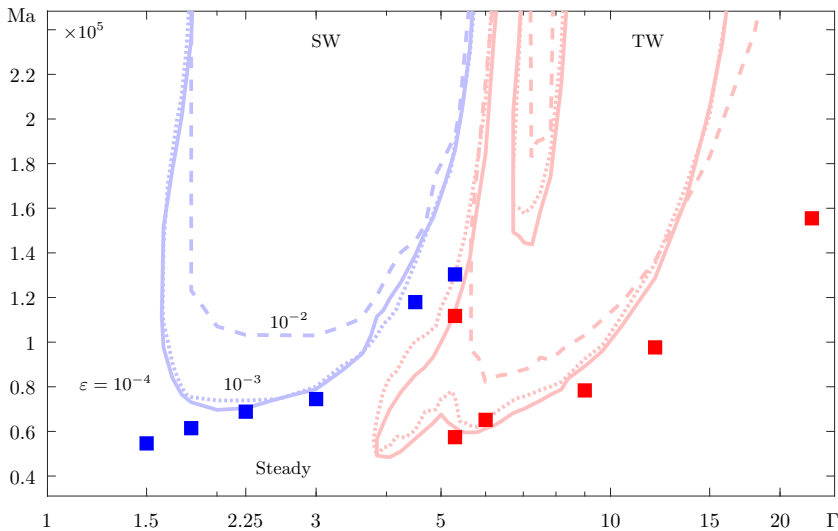


FIG. 16. Stability map in terms of Γ and Ma showing the primary Hopf bifurcation to SW (blue) and TW (red) modes with different heating rates: $\epsilon = 10^{-4}$ K/s (solid), 10^{-3} K/s (dotted), and 10^{-2} K/s (dashed). The markers show the critical Ma for SW (blue) and TW (red) determined for the melting of *n*-octadecane in microgravity; reproduced from Ref. [26].

For the intermediate range of Γ , simulations were performed in a rectangular container with $\Gamma \simeq 5.29$. At low Ma , the flow is steady, and a small-scale SMC state appears. With increasing Ma , this vortical structure becomes unstable to the TW mode. The TWs appear for a limited part of the melting process and disappear again before its completion. The final thermocapillary flow in this case is a steady vortical structure. At a certain value of Ma , the evolution of the flow becomes completely steady, with the initial small-scale SMC state developing directly into a large-scale structure. This steady regime persists only over a small range of Ma and becomes unstable to the SW mode at larger values.

Figure 16 summarizes the different flow regimes observed during melting in terms of Ma and Γ . The critical boundaries for oscillatory flow (adapted from Ref. [26]) are indicated by markers: red for the TW mode, blue for the SW mode. The stability map of Fig. 3 for increasing ΔT is superimposed on these data points. In addition to the (solid) curve calculated with $\epsilon = 10^{-4}$ K/s, the critical curves obtained with $\epsilon = 10^{-3}$ K/s (dotted) and 10^{-2} K/s (dashed) are included for comparison.

Overall, there is reasonable agreement between the stability regions calculated for the ideal rectangular case, and those observed during the phase change. Note that even the narrow region of steady solutions observed during melting for $\Gamma \simeq 5.29$ aligns fairly well with the corresponding region of steady solutions found in Sec. III. The most notable differences are observed at large Γ where the critical Ma values found during melting are well below the bifurcation curve for a rectangular container of liquid. As discussed in more detail below, this suggests that the advancing solid/liquid front has a destabilizing effect on the flow dynamics.

We use these stability maps to explain the dynamics observed during melting, and make use of the *effective* aspect ratio Γ_{eff} and Marangoni number Ma_{eff} of the liquid phase to define the relevant paths in parameter space. The analysis is divided into the cases of small, large and intermediate Γ containers.

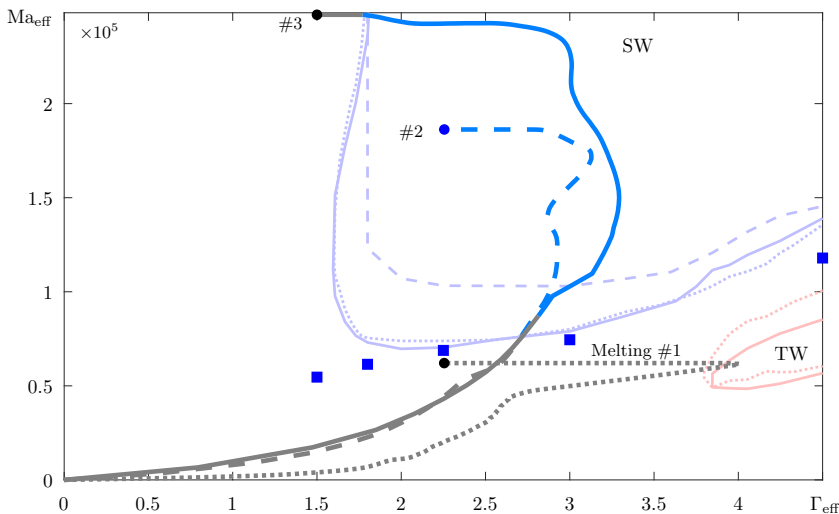


FIG. 17. Melting paths in effective parameters (Γ_{eff} , Ma_{eff}) for three cases with dynamics representative of small-aspect-ratio containers. Melting no. 1 (dotted curve): $\Gamma = 2.25$, $\text{Ma} \simeq 6.21 \times 10^4$ ($H = 10$ mm, $\Delta T = 10$ K). Melting no. 2 (dashed curve): $\Gamma = 2.25$, $\text{Ma} = 1.86 \times 10^5$ ($H = 10$ mm, $\Delta T = 30$ K). Melting no. 3 (solid curve): $\Gamma = 1.5$, $\text{Ma} \simeq 2.48 \times 10^5$ ($H = 15$ mm, $\Delta T = 40$ K). The nature of the thermocapillary flow is indicated by color: steady (gray), SWs (blue).

C. Small-aspect-ratio containers

Figure 17 shows the paths traced by the melting process in the parameter space (Γ_{eff} , Ma_{eff}) for three cases that are representative of the dynamics in small-aspect-ratio containers. The nature of the thermocapillary flow observed during the melting process is indicated: steady solutions in gray and SWs in blue. The associated temperature profiles δT_1 are shown in Fig. 18, with insets illustrating the temperature field and the streamlines of the flow in the liquid at selected times during the phase change.

Melting no. 1 is representative of the (quasi-)steady dynamics in small-aspect-ratio containers discussed in Sec. 4 of Ref. [26]. The melting is analyzed in a container of $\Gamma = 2.25$ ($H = 10$ mm) subjected to a moderate $\text{Ma} \simeq 6.21 \times 10^4$ ($\Delta T = 10$ K). The curves corresponding to this case are labeled in both figures.

As described by these authors, heat transport is dominated by thermal diffusion at the beginning of the phase change. As soon as the solid/liquid front separates enough from the hot boundary, the thermocapillary effect drives convection in an initially thin region (compared to H) near the free surface. Melting is enhanced in this region, which locally accelerates the progression of the solid/liquid front; see the insets of Fig. 18. During this stage, Γ_{eff} of the thermocapillary layer is generally larger than Γ ; see the dotted curve of Fig. 17. Consequently, the flow structure is that of an SMC state, as seen in the streamlines of the insets. Recall that this structure is typical of large-aspect-ratio containers; see Sec. III B, and Sec. 4 of Ref. [26]. During this initial part of the melting, the cold boundary for the liquid is essentially determined by the advancing solid/liquid front. The advancement of the melting front near the bottom wall is driven mainly by thermal diffusion.

As the thermocapillary layer evolves, the solid/liquid front reaches the cold wall. After this, the liquid depth along this boundary increases with time; see the insets. It is near this point of the melting process when Γ_{eff} takes its maximum value and Ma_{eff} is close to the nominal value of 6.21×10^4 ; see Fig. 17. From this point onward, Γ_{eff} slowly decreases and the vortical structure moves toward the cold wall. The number of vortices is progressively reduced through the absorption of the smallest vortex (near the cold wall) by its neighbor, until the final state with two vortices is reached. At the

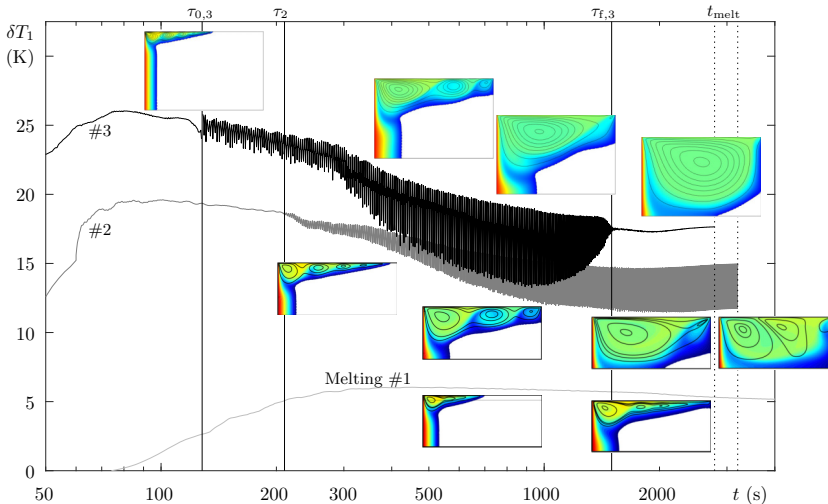


FIG. 18. Temperature $\delta T_1 = T_1 - T_M$ during meltings no. 1–3 (labeled). The vertical lines mark the appearance/cessation of oscillatory flow and the melting completion (dashed); these are labeled as $\tau_{0,\#}$, $\tau_{f,\#}$ and τ_{melt} , respectively, where $\#$ refers to the melting number. The insets show the temperature and velocity within the liquid at increasing times.

completion of melting, which occurs by 9185 s [32], the final selected pattern is analogous to that of Fig. 5, with a large vortex shifted toward the hot wall, and a small vortex near the cold side of the thermocapillary interface, similar to the solution discussed in Refs. [15,16]. For this value of Ma , the flow remains steady, as shown in Fig. 18. This steady flow is consistent with the path traced by the effective parameters in Fig. 17.

Melting no. 2 is representative of the oscillatory flow observed during melting in small-aspect-ratio containers; this was discussed in Sec. 4 of Ref. [26]. This case is analyzed for the same aspect ratio $\Gamma = 2.25$ ($H = 10$ mm) but with larger thermal forcing of $\text{Ma} \simeq 1.86 \times 10^5$ ($\Delta T = 30$ K). The corresponding curves are labeled in Figs. 17 and 18.

The overall progression of the phase change is similar to that of $\text{Ma} \simeq 6.21 \times 10^4$, but with the total melting time reduced to $t_{\text{melt}} = 3200$ s, as expected for a value of Ma that is three times larger; see the associated vertical dotted line of Fig. 18. Again, the flow in the liquid initially shows two regions: the thermocapillary-driven layer near the free surface and the diffusion-dominated region near the bottom wall. The localized SMC state contains four vortices.

After approximately 200 s, the temperature signal of Fig. 18 (dark gray) reveals a transition to the SW mode; marked by a color change from gray to blue in Fig. 17. As the figure shows, this transition, when parametrized by Γ_{eff} and Ma_{eff} , occurs between the dotted and dashed curves obtained with the liquid-only simulations of Sec. III, in very good agreement. Recall that these curves were calculated for $\varepsilon = 10^{-2}$ K/s and $\varepsilon = 10^{-3}$ K/s, respectively. The faster of these two ramp rates corresponds to increasing (instantaneous) Ma with $d(\text{Ma})/dt = \gamma L \varepsilon / (\mu_L \alpha) \simeq 60$ and the slower one to $d(\text{Ma})/dt = 6$. For melting no. 2, the phase change is completed by $t_{\text{melt}} = 3200$ s, which provides an estimate of $d \text{Ma}_{\text{eff}}/dt \approx \text{Ma}/t_{\text{melt}} \simeq 58$. The similarity of these rate estimates helps explain the good agreement.

At all times after the transition, the flow in the liquid is oscillatory with dynamics characteristic of the SW mode. When melting is finished, $(\Gamma_{\text{eff}}, \text{Ma}_{\text{eff}}) = (\Gamma, \text{Ma})$ and the system lies within the region of stable SWs found in Sec. III, consistent with the observed behavior. As discussed in Sec. 4 of Ref. [26], the oscillatory thermocapillary flow has a natural frequency that decreases with time. The final SW frequency was found to be $f \simeq 0.07$ Hz, which is in reasonable agreement with the

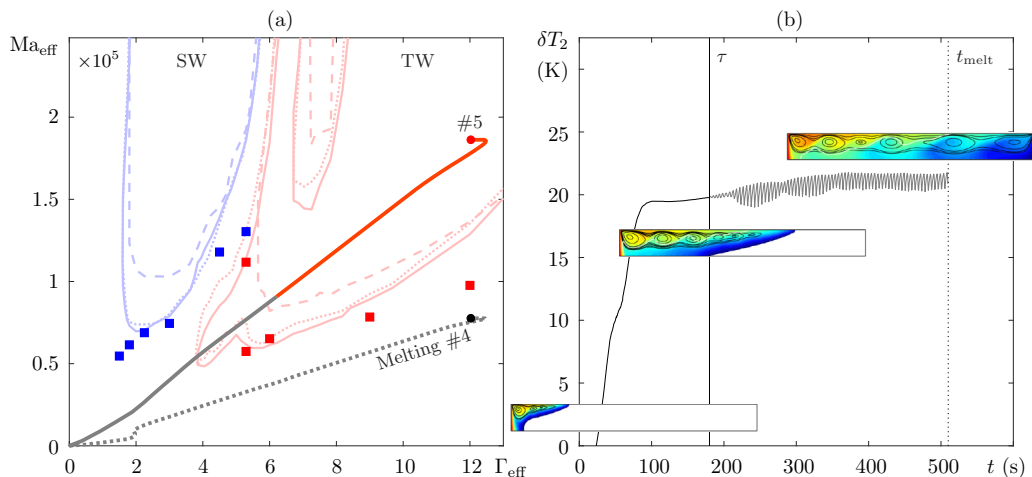


FIG. 19. (a) Melting paths in effective parameters (Γ_{eff} , Ma_{eff}) for two choices of Ma in a container of $\Gamma = 12$, which are representative of the dynamics in the large-aspect-ratio regime. Melting no. 4 (dotted curve): $\text{Ma} \simeq 7.76 \times 10^4$ ($\Delta T = 12.5$ K). Melting no. 5 (solid curve): $\text{Ma} \simeq 1.86 \times 10^5$ ($\Delta T = 30$ K). The nature of the thermocapillary flow is indicated by color: steady (gray) and TW (red). (b) Temperature δT_2 during melting no. 5, with vertical lines marking the appearance of oscillatory flow and the completion of melting (at τ , τ_{melt}). Insets illustrate the temperature and velocity at selected moments during melting.

frequency $f \simeq 0.08$ Hz obtained in Sec. III A for the same Γ and Ma ; this value can be extracted from the spectrogram of Fig. 4(b) for $\Delta T = 30$ K.

Finally, melting no. 3 is selected to examine another type of behavior discussed in Ref. [26], where the phase change is characterized by two transitions. As observed for $\Gamma = 1.5$, there is one transition from steady flow to the SW mode, then another back to steady flow. The simulation included here is for a large thermal forcing of $\text{Ma} \simeq 2.48 \times 10^5$ ($\Delta T = 40$ K). As seen in Fig. 18 (black curve), the flow begins to oscillate approximately 100 s after melting is initiated; labeled as $\tau_{0,3}$. These oscillations last for a significant part of the melting process, but disappear at $t \simeq 1600$ s; labeled as $\tau_{f,3}$. As with the other cases, the transitions can be explained in terms of the path traced by (Γ_{eff} , Ma_{eff}); this path is shown in Fig. 17 (solid line). The first transition can be observed just past the critical curve of the SW mode. Note that, for this simulation, melting finishes after 2785 s, which leads to the estimate $d \text{Ma}_{\text{eff}}/dt \simeq \text{Ma}/t_{\text{melt}} \approx 88$ that partly explains the delayed appearance of SWs. The second transition back to steady flow occurs at the point marked as $\tau_{f,3}$ in Fig. 18. It can be seen from Fig. 17 that this transition (from blue to gray) coincides with the effective parameters crossing the upper part of the critical curve. The final pattern lies in a region of stable steady flow, consistent with the analysis of Sec. III.

D. Large-aspect-ratio containers

An analogous set of results is now presented for representative cases in large-aspect-ratio containers. Figure 19(a) shows the paths traced by meltings nos. 4 and 5 in the space of effective parameters (Γ_{eff} , Ma_{eff}); see Table IV. As before, the nature of the observed thermocapillary flow is indicated by the color: steady (gray) and TW (red). The temperature $\delta T_2 = T_2 - T_M$ during melting no. 5 is included in Fig. 19(b), with vertical lines marking the appearance of oscillatory flow and the completion of melting (labeled as τ and τ_{melt} , respectively). The insets show the temperature and velocity at selected times during melting.

Melting no. 4 illustrates the type of steady thermocapillary flow found in large containers in Sec. 3 of Ref. [26]. The phase transition is analyzed for a moderate level of thermal forcing,

$Ma \simeq 7.76 \times 10^4$ ($\Delta T = 12.5$ K), in a container of $\Gamma = 12$. As discussed in that reference, Γ_{eff} in large containers rapidly grows to large values and SMC states are consistently observed. This is consistent with the path of effective parameters shown (dotted curve) in Fig. 19(a), which does not cross any of the critical boundaries for oscillatory flow found in Sec. III.

Melting no. 5, with a larger value of $Ma \simeq 1.86 \times 10^5$ ($\Delta T = 30$ K), does exhibit a transition to oscillatory flow in the form of TWs. As soon as the solid/liquid front separates enough from the hot boundary, the thermocapillary effect drives convection near the free surface; see the lower left inset of Fig. 19(b). As time passes, the thickness of the thermocapillary layer grows until it spans the full cell height. From this time onward, the solid/liquid front maintains a similar overall shape as it advances across the container to the cold wall; see the middle inset of Fig. 19(b). During this interval of the melting process, the SMC flow acquires an increasing number of vortices. At some moment [labeled as τ in Fig. 19(b)], the vortical structure begins to oscillate, and a TW is generated. As described earlier, the TW mode is characterized by the cyclic creation of vortices at the cold boundary (i.e., at the solid/liquid interface or the cold wall) that travel toward the hot wall. The instability mechanism responsible for generating TWs in high Pr liquids was discussed by Smith [21].

With this value of Ma , the solid is completely melted by $t_{\text{melt}} = 510$ s [32], which leads to the estimate $dMa/dt \approx Ma/t_{\text{melt}} \simeq 365$. This higher rate of increase explains the more pronounced delay seen in Fig. 19(a) for the appearance of TW, compared to the onset predicted for the ideal rectangular case. The dominant frequency of the TWs during melting was found to be $f \simeq 0.2$ Hz [26] and to be nearly independent of Ma over a wide range, consistent with the spectrograms of Fig. 10. In fact, Fig. 19(b), which was obtained for the same aspect ratio of $\Gamma = 12$, indicates a dominant frequency of $f \simeq 0.2$ Hz, which agrees very well with the value observed during melting.

Finally, we remark on the differences between the onset of TWs obtained in Ref. [26] and the critical curves calculated in this work for large Γ . Figure 19(a) shows that the relatively good agreement over small and intermediate aspect ratios is diminished at larger Γ . The difference suggests that, for a given (nominal) Γ and Ma , the presence of dynamic boundary conditions during melting has a destabilizing effect, with the critical curve for TW shifted to lower values of Ma compared to the equivalent container of pure liquid.

E. Intermediate-aspect-ratio containers

The study is completed by exploring melting in intermediate-aspect-ratio containers. As described in Sec. IV B, this intermediate regime is characterized by the appearance of both TWs and SWs, depending on the value of Ma . Again, the melting dynamics are understood by tracing the paths of $(\Gamma_{\text{eff}}, Ma_{\text{eff}})$. Meltings nos. 6–8 can be compared to the predicted transitions in the absence of a phase change, and do exhibit the initial bifurcation to TWs (path no. 6), the intermediate range of moderate Ma where the melting becomes steady again (path no. 7), and the final transition to the SW mode at larger Ma (path no. 8). The associated values of (Γ, Ma) are labeled and located by circular markers in Fig. 19(a). Note that there is region of steady flow (marker no. 7) between the critical curve for TW and SWs at moderate Ma .

Figure 20 shows the melting paths superimposed on the stability map obtained in Sec. III. The path of melting no. 6 in effective parameters explains the appearance of TWs at a certain point of the melting process. In this case, they persist beyond the completion of melting since the values of Γ and Ma lie within the region of stable TWs.

If Ma is increased, these TWs may appear only during a limited portion of the melting [26] as the upper part of the critical boundary for TWs is crossed. For example, melting no. 7 traces a path that ends within the region of predicted steady flow and the final observed pattern is steady. Note that the definition of Γ_{eff} used here may overestimate the maximum value of the “equivalent” aspect ratio since this path also predicts the temporary appearance of TWs, which are not observed during that melting process. Alternatively, it may simply be that the short time spent in this (unstable) part of the diagram is insufficient for TWs to properly develop.

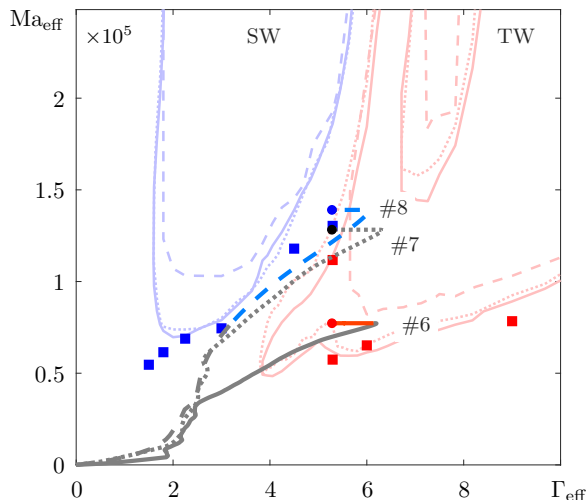


FIG. 20. Melting paths in effective parameters (Γ_{eff} , Ma_{eff}) for intermediate-aspect-ratio containers of $\Gamma = 5.29$ ($H = 4.25$ mm) and three Ma values: $\text{Ma} \simeq 7.76 \times 10^4$ (melting no. 6, solid curve, $\Delta T = 12.5$ K), $\text{Ma} \simeq 1.29 \times 10^5$ (melting no. 7, dotted curve, $\Delta T = 20.75$ K), and $\text{Ma} \simeq 1.40 \times 10^4$ (melting no. 8, dashed curve, $\Delta T = 22.5$ K). In all cases, the type of thermocapillary flow is color-coded: steady (gray), SW (blue), TW (red).

Finally, the path of melting no. 8 shows the selection of SWs at larger Ma. Note that, as with the TW instability in large-aspect-ratio containers, the threshold for SW to appear during the melting process is lower than in the corresponding container of pure liquid. While much of this can be explained by the dynamics of the melting front, as reflected by Ma_{eff} and Γ_{eff} , other differences likely result from the different numerical models used.

V. CONCLUSIONS

A detailed numerical investigation of pattern selection for thermocapillary-driven flows in rectangular containers in microgravity was presented. The flow was analysed for the case of liquid *n*-octadecane, which has a high Prandtl number of $\text{Pr} = 52.53$, due to its relevance to anticipated [55] and recent microgravity experiments [29–31]. The key bifurcation sets were analyzed in Sec. III and the associated patterns were organized in terms of the aspect ratio (Γ) and the applied Marangoni number (Ma). The results were summarized with a stability map showing regions of steady solutions, standing waves (SW) and traveling waves (TW).

In small-aspect-ratio containers, the thermocapillary flow undergoes a transition from a steady to an oscillatory SW mode as Ma is varied. The primary instability is due to a subcritical Hopf bifurcation and is accompanied by a secondary saddle-node bifurcation. These two critical curves delimit a bistable region where both steady flow and SWs can be found, depending on initial conditions. The structure of the base flow is characterized by a small number of vortices, which are biased toward the hot wall, consistent with the observations of Refs. [17] and [18]. The emergence of SWs from this base flow causes the vortices to pulsate back and forth, a motion driven by the interaction between cool perturbations, which are repeatedly siphoned off from the cold wall, and the thermocapillary interface near the hot wall. The spectrum of SW solutions reveals a dominant frequency that increases with the level of thermal forcing (Ma) and with Γ .

In large-aspect-ratio containers, the principal transition is from steady flow to an oscillatory TW mode as Ma is increased. This instability is due to a supercritical Hopf bifurcation whose critical Ma value increases with Γ . Prior to this instability, the steady thermocapillary flow exhibits structures

that evolve from the steady return flow solution [19] at low Ma to a steady multicellular structure (SMC) [2,27]. This SMC state constitutes the base flow for the development of TWs, which are characterized by the cyclic creation of vortices at the cold side that detach and travel toward the hot side. A spectral analysis shows that the TW frequency is largely insensitive to Ma while increasing with Γ .

In intermediate-aspect-ratio containers, a more complicated picture of pattern selection is found. Both steady and oscillatory flow—in the form of either TWs or SWs—can be obtained depending on Γ and Ma . For these containers, the SW mode appears via a supercritical Hopf bifurcation, while the TW arises in a subcritical Hopf bifurcation. This primary TW instability is accompanied by a secondary saddle-node bifurcation and together they define a bistable region supporting both steady and TW solutions.

The results obtained for rectangular containers of liquid are used in Sec. IV to understand the various dynamics observed during the melting process in microgravity. The phase change is described using an enthalpy-porosity formulation of the Navier-Stokes equations [70], which models the coexisting solid and liquid states as a single domain with physical properties depending on temperature and changing sharply across the solid/liquid front. The initially solid n -octadecane is melted by applying a temperature difference ΔT across the (isothermal) lateral walls. The temporal evolution of the melting process and associated flow is then related to the stability map of Sec. III by defining an effective aspect ratio Γ_{eff} and an effective Marangoni number Ma_{eff} to characterize the changing liquid domain.

Good agreement is found between the transitions observed during melting and those located in rectangular containers of liquid by considering the paths traced by these effective parameters Γ_{eff} and Ma_{eff} . For containers of small Γ , this correspondence provides a qualitative explanation for why the convective flow at low-to-moderate Ma is initially characterized by the evolution from SMC states to large-scale vortical structures. For larger Ma , both the transition from steady flow to SWs and the subsequent return of steady flow are consistent with the results obtained for rectangular containers of liquid. For containers of large Γ , the transition from steady return flow (SRF) to SMC states, and the ensuing loss of stability to TWs, are likewise consistent with the results of Sec. III. Furthermore, the measured TW frequencies are in agreement, including their dependence on Γ and their insensitivity to Ma . Containers of intermediate aspect ratio are considered as well, using three distinct melting paths for $\Gamma \simeq 5.29$. The transition from steady flow to TWs, the return of steady flow at moderate Ma , and the final transition to SWs can be explained quite well using effective parameters to map the dynamics of the melting process onto the results obtained in Sec. III for ideal rectangular volumes of liquid.

ACKNOWLEDGMENTS

This work was supported by the Ministerio de Ciencia e Innovación under Project No. PID2020-115086GB-C31, and by the Spanish Support and Operations Centre (E-USOC), Center for Computational Simulation (CCS).

-
- [1] J. C. Brice, *Crystal Growth Processes*, Blackie & Son Ltd., Glasgow and London 1986 (distributed in the USA by Halsted Press, a Division of John Wiley and Sons Inc., New York).
 - [2] D. Schwabe and A. Scharmann, Some evidence for the existence and magnitude of a critical Marangoni number for the onset of oscillatory flow in crystal growth melts, *J. Cryst. Growth* **46**, 125 (1979).
 - [3] M. Lappa, On the formation and propagation of hydrothermal waves in liquid layers with phase change, *Comput. Fluids* **172**, 741 (2018).
 - [4] W. A. Sirignano and I. Glassman, Flame spreading above liquid fuels: Surface tension driven flows, *Combust. Sci. Technol.* **1**, 307 (1970).

- [5] F. J. Higuera, Liquid-fuel thermocapillary flow induced by a spreading flame, *J. Fluid Mech.* **473**, 349 (2002).
- [6] S. K. Samanta, *Interdisciplinary Issues in Materials Processing and Manufacturing* (American Society of Mechanical Engineers, New York, 1987).
- [7] K. C. Mills, B. J. Keene, R. F. Brooks, and A. Shirali, Marangoni effects in welding, *Philos. Trans. R. Soc. London, Ser. A* **356**, 911 (1998).
- [8] S. Z. Shuja, B. S. Yilbas, and O. Momin, Laser repetitive pulse heating and melt pool formation at the surface, *J. Mech. Sci. Technol.* **25**, 479 (2011).
- [9] P. Erhard and S. H. Davis, Nonisothermal spreading of liquid drops on horizontal planes, *J. Fluid Mech.* **229**, 365 (1991).
- [10] R. S. Subramanian, The motion of bubbles and drops in reduced gravity, in *Transport Processes in Bubbles, Drops and Particles* (Hemisphere, 1992).
- [11] L. Rosenfeld, O. M. Lavrenteva, and A. Nir, On the thermocapillary motion of partially engulfed compound drops, *J. Fluid Mech.* **626**, 263 (2009).
- [12] J. R. Mac Intyre, J. M. Gomba, C. A. Perazzo, P. G. Correa, and M. Sellier, Thermocapillary migration of droplets under molecular and gravitational forces, *J. Fluid Mech.* **847**, 1 (2018).
- [13] H. C. Kuhlmann and S. Albensoeder, Three-dimensional flow instabilities in a thermocapillary-driven cavity, *Phys. Rev. E* **77**, 036303 (2008).
- [14] A. Zebib, G. M. Homsy, and E. Meiburg, High Marangoni number convection in a square cavity, *Phys. Fluids* **28**, 3467 (1985).
- [15] B. M. Carpenter and G. M. Homsy, High Marangoni number convection in a square cavity: Part II, *Phys. Fluids* **2**, 137 (1990).
- [16] L. J. Peltier and S. Biringen, Time-dependent thermocapillary convection in a rectangular cavity: Numerical results for a moderate Prandtl number fluid, *J. Fluid Mech.* **257**, 339 (1993).
- [17] A. K. Sen and S. H. Davis, Steady thermocapillary flows in two-dimensional slots, *J. Fluid Mech.* **121**, 163 (1982).
- [18] M. Strani, R. Piva, and G. Graziani, Thermocapillary convection in a rectangular cavity: Asymptotic theory and numerical simulation, *J. Fluid Mech.* **130**, 347 (1983).
- [19] C. Chub and W. Wuest, Experiments on the transition from the steady to the oscillatory Marangoni-convection of a floating zone under reduced gravity effect, *Acta Astronaut.* **6**, 1073 (1979).
- [20] M. K. Smith and S. H. Davis, Instabilities of dynamic thermocapillary liquid layers. Part 1. Convective instabilities, *J. Fluid Mech.* **132**, 119 (1983).
- [21] M. K. Smith, Instability mechanisms in dynamic thermocapillary liquid layers, *Phys. Fluids* **29**, 3182 (1986).
- [22] P. Laure, B. Roux, and H. Ben Hadid, Nonlinear study of the flow in a long rectangular cavity subjected to thermocapillary effect, *Phys. Fluids A* **2**, 516 (1990).
- [23] J.-F. Mercier and C. Normand, Influence of the Prandtl number on the location of recirculation eddies in thermocapillary flows, *Int. J. Heat Mass Transf.* **45**, 793 (2002).
- [24] J. Priede and G. Gerbeth, Convective, absolute, and global instabilities of thermocapillary-buoyancy convection in extended layers, *Phys. Rev. E* **56**, 4187 (1997).
- [25] V. M. Shevtsova, A. A. Nepomnyashchy, and J. C. Legros, Thermocapillary-buoyancy convection in a shallow cavity heated from the side, *Phys. Rev. E* **67**, 066308 (2003).
- [26] P. Salgado Sanchez, J. M. Ezquerro, J. Fernandez, and J. Rodriguez, Thermocapillary effects during the melting of phase-change materials in microgravity: Steady and oscillatory flow regimes, *J. Fluid Mech.* **908**, A20 (2021).
- [27] S. Madruga and C. Mendoza, Enhancement of heat transfer rate on phase change materials with thermocapillary flows, *Eur. Phys. J. Spec. Top.* **226**, 1169 (2017).
- [28] S. Madruga and C. Mendoza, Heat transfer performance and melting dynamic of a phase change material subjected to thermocapillary effects, *Int. J. Heat Mass Transf.* **109**, 501 (2017).
- [29] J. M. Ezquerro, A. Bello, P. Salgado Sanchez, A. Laveron-Simavilla, and V. Lapuerta, The Thermocapillary Effects in Phase Change Materials in Microgravity experiment: Design, preparation and execution of a parabolic flight experiment, *Acta Astronaut.* **162**, 185 (2019).

- [30] J. M. Ezquerro, P. Salgado Sanchez, A. Bello, J. Rodriguez, V. Lapuerta, and A. Laveron-Simavilla, Experimental evidence of thermocapillarity in phase change materials in microgravity: Measuring the effect of Marangoni convection in solid/liquid phase transitions, *Int. Commun. Heat Mass Transfer* **113**, 104529 (2020).
- [31] P. Salgado Sanchez, J. M. Ezquerro, J. Porter, J. Fernandez, and I. Tinao, Effect of thermocapillary convection on the melting of phase change materials in microgravity: Experiments and simulations, *Int. J. Heat Mass Transf.* **154**, 119717 (2020).
- [32] P. Salgado Sanchez, J. M. Ezquerro, J. Fernandez, and J. Rodriguez, Thermocapillary effects during the melting of phase change materials in microgravity: Heat transport enhancement, *Int. J. Heat Mass Transf.* **163**, 120478 (2020).
- [33] W. R. Humphries and E. I. Griggs, *A Design Handbook for Phase Change Thermal Control and Energy Storage Devices* (United States, 1977).
- [34] M. Giangi, F. Stella, E. Leonardi, and G. De Vahl Davis, A numerical study of spñodofocation in the presence of a free surface under microgravity conditions, *Numer. Heat Transfer A* **41**, 579 (2002).
- [35] T. D. Swanson and G. C. Birur, NASA thermal control technologies for robotic spacecraft, *Appl. Therm. Eng.* **23**, 1055 (2003).
- [36] G. Xiaohong, S. Xiange, Z. Miao, and T. Dawei, Influence of void ratio on thermal stress of PCM canister for heat pipe receiver, *Appl. Therm. Eng.* **94**, 615 (2012).
- [37] L. Cabeza, H. Mehling, S. Hiebler, and F. Ziegler, Heat transfer enhancement in water when used as PCM in thermal energy storage, *Appl. Therm. Eng.* **22**, 1141 (2002).
- [38] H. M. Ettouney, I. Alatiqi, M. Al-Sahali, and S. A. Al-Ali, Heat transfer enhancement by metal screens and metal spheres in phase change energy storage systems, *Renew. Energy* **29**, 841 (2004).
- [39] F. Agyenim, P. Eames, and M. Smyth, A comparison of heat transfer enhancement in a medium temperature thermal energy storage heat exchanger using fins, *Solar Energy* **83**, 1509 (2009).
- [40] D. Fernandes, F. Pitie, G. Caceres, and J. Baeyens, Thermal energy storage: “How previous findings determine current research priorities”, *Energy* **39**, 246 (2012).
- [41] A. Atal, Y. Wang, M. Harsha, and S. Sengupta, Effect of porosity of conducting matrix on a phase change energy storage device, *J. Heat Mass Transfer* **93**, 9 (2016).
- [42] S. F. Hosseinizadeh, A. A. R. Darzi, and F. L. Tan, Numerical investigations of unconstrained melting of nano-enhanced phase change material (NEPCM) inside a spherical container, *Int. J. Therm. Sci.* **51**, 77 (2012).
- [43] N. S. Dhaidan, J. M. Khodadadi, T. A. Al-Hattab, and S. M. Al-Mashat, Experimental and numerical investigation of melting of NePCM inside an annular container under a constant heat flux including the effect of eccentricity, *Int. J. Heat Mass Transf.* **67**, 455 (2013).
- [44] C. Gau and R. Viskanta, Melting and solidification of a pure metal on a vertical wall, *Trans. ASME* **108**, 174 (1986).
- [45] S. K. Roy and S. Sengupta, Gravity-assisted melting in a spherical enclosure: Effects of natural convection, *Int. J. Heat Mass Transf.* **33**, 1135 (1990).
- [46] Y. Wang, A. Amiri, and K. Vafai, An experimental investigation of the melting process in a rectangular enclosure, *Int. J. Heat Mass Transf.* **42**, 3659 (1999).
- [47] J. M. Khodadadi and Y. Zhang, Effects of buoyancy-driven convection on melting within spherical containers, *Int. J. Heat Mass Transf.* **44**, 1605 (2001).
- [48] H. Shokouhmand and B. Kamkari, Experimental investigation on melting heat transfer characteristics of lauric acid in a rectangular thermal storage unit, *Exp. Therm. Fluid Sci.* **50**, 201 (2013).
- [49] N. S. Dhaidan and J. M. Khodadadi, Melting and convection of phase change materials in different shape containers: A review, *Renew. Sustain. Energy Rev.* **43**, 449 (2015).
- [50] P. Salgado Sanchez, J. M. Ezquerro, J. Porter, J. Fernandez, J. Rodriguez, I. Tinao, V. Lapuerta, A. Laveron-Simavilla, X. Ruiz, F. Gavalda, M. M. Mounir Bou-Ali, and J. Ortiz, The effect of thermocapillary convection on PCM melting in microgravity: Results and expectations, in *Proceedings of the 72th International Astronautical Conference (IAC)* (2020).

- [51] A. Borshchak Kachalov, P. Salgado Sánchez, J. Porter, and J. Ezquerro, The combined effect of natural and thermocapillary convection on the melting of phase change materials in rectangular containers, *Int. J. Heat Mass Transf.* **168**, 120864 (2021).
- [52] R. Varas, P. Salgado Sánchez, J. Porter, J. Ezquerro, and V. Lapuerta, Thermocapillary effects during the melting in microgravity of phase change materials with a liquid bridge geometry, *Int. J. Heat Mass Transf.* **178**, 121586 (2021).
- [53] N. Martínez, P. Salgado Sanchez, J. Porter, and J. M. Ezquerro, Effect of surface heat exchange on phase change materials melting with thermocapillary flow in microgravity, *Phys. Fluids* **33**, 083611 (2021).
- [54] A. Borshchak Kachalov, P. Salgado Sánchez, U. Martínez, J. Ezquerro, and J. Fernández, Optimization of thermocapillary-driven melting in trapezoidal and triangular geometry in microgravity, *Int. J. Heat Mass Transf.* **185**, 122427 (2022).
- [55] A. Laverón, Experiment Scientific Requirement (ESR) document: Effect of Marangoni convection on heat transfer in phase change materials, Ref: ESA-HRE-ESR-Marangoni in PCM, Iss. 1, Rev. 2 (2021).
- [56] L. D. Landau and E. M. Lifshitz, *Fluid Mechanics* (Pergamon Books, 1987).
- [57] J. M. Montanero, C. Ferrero, and V. M. Shevtsova, Experimental study of the free surface deformation due to thermal convection in liquid bridges, *Exp. Fluids* **45**, 1087 (2008).
- [58] V. Shevtsova, A. Mialdun, C. Ferrera, M. Ermakov, M. G. Cabezas, and J. Montanero, Subcritical and oscillatory dynamic surface deformations in non-cylindrical liquid bridges, *Fluid Dyn. Mater Process.* **4**, 43 (2008).
- [59] D. W. Camp, National technical paper 1071-1080, NASA Technical Reports (1977).
- [60] I. Harari and T. Hughes, What are C and h ?: Inequalities for the analysis and design of finite element methods, *Comput. Methods Appl. Mech. Eng.* **97**, 157 (1992).
- [61] R. Codina, A discontinuity-capturing crosswind-dissipation for the finite element solution of the convection-diffusion equation, *Comput. Methods Appl. Mech. Eng.* **110**, 325 (1993).
- [62] R. Mannella, F. Moss, and P. V. E. McClintock, Postponed bifurcations of a ring-laser model with a swept parameter and additive colored noise, *Phys. Rev. A* **35**, 2560 (1987).
- [63] N. Berglund and B. Gentz, Pathwise description of dynamic pitchfork bifurcations with additive noise, *Probab. Theory Relat. Fields* **122**, 341 (2002).
- [64] Y. Do and J. M. Lopez, Slow passage through multiple bifurcation points, *Discrete Contin. Dyn. Syst. B* **18**, 95 (2013).
- [65] P. Mandel and T. Erneux, The slow passage through a steady bifurcation: Delay and memory effects, *J. Stat. Phys.* **48**, 1059 (1987).
- [66] S. M. Baer, T. Erneux, and J. Rinzel, The slow passage through a hopf bifurcation: Delay, memory effects, and resonance, *SIAM J. Appl. Math.* **49**, 55 (1987).
- [67] E. Bucchignani and D. Mansutti, Horizontal thermal convection in a shallow cavity: Oscillatory regimes and transition to chaos, *Int. J. Numer. Methods Heat Fluid Flow* **10**, 179 (1999).
- [68] E. Bucchignani and D. Mansutti, Horizontal thermocapillary convection of succinonitrile: Steady state, instabilities and transition to chaos, *Phys. Rev. E* **69**, 056319 (2004).
- [69] K. Li, B. Xun, and W. R. Hu, Some bifurcation routes to chaos of thermocapillary convection in two-dimensional liquid layers of finite extent, *Phys. Fluids* **28**, 054106 (2016).
- [70] V. R. Voller, M. Cross, and N. C. Markatos, An enthalpy method for convection/diffusion phase change, *Int. J. Numer. Methods Eng.* **24**, 271 (1987).
- [71] P. W. Egolf and H. Manz, Theory and modeling of phase change materials with and without mushy regions, *Int. J. Heat Mass Transf.* **37**, 2917 (1994).